

A model for two-proton emission induced by electron scattering

Marta Anguiano and Giampaolo Co'

Dipartimento di Fisica, Università di Lecce and I.N.F.N. sez. di Lecce, I-73100 Lecce, Italy

Antonio M. Lallena

Departamento de Física Moderna, Universidad de Granada, E-18071 Granada, Spain

Abstract

A model to study two-proton emission processes induced by electron scattering is developed. The process is induced by one-body electromagnetic operators acting together with short-range correlations, and by two-body Δ currents. The model includes all the diagrams containing a single correlation function. A test of the sensitivity of the model to the various theoretical inputs is done. An investigation of the relevance of the Δ currents is done by changing the final state angular momentum, excitation energy and momentum transfer. The sensitivity of the cross section to the details of the correlation function is studied by using realistic and schematic correlations. Results for ^{12}C , ^{16}O and ^{40}Ca nuclei are presented.

PACS number(s): 21.10.Ft, 21.60.-n

1 INTRODUCTION

This article belongs to a series dedicated to the study of the effects of the short range correlations (SRC) in processes induced by electromagnetic probes on atomic nuclei [1]-[3].

The SRC are produced by the strong repulsion of the bare nucleon-nucleon potential at internucleon distances smaller than ~ 0.5 fm. Every nuclear structure calculation that uses bare nucleon-nucleon potentials requires the presence of SRC, however, in medium-heavy nuclei, phenomena which can be unambiguously attributed to them have not yet been identified.

A well known effect of the SRC is the depletion of the occupation probability of the quasi-hole states. Unfortunately, an analogous effect is also produced by the coupling of the single particle wave function with the low-lying phonons generated by collective nuclear vibrations. The inclusion of both effects seems to be necessary to account for the empirical occupation numbers [4, 5].

A more striking, and even better known, effect of the SRC is the various order of magnitude enhancement of the nucleon momentum distribution $n(k)$ at high momentum values [6]. Unfortunately, this quantity is not directly observable. It is therefore necessary to find measurable quantities related to it, hoping that they are sufficiently sensitive to $n(k)$ to allow for an unambiguous identification of the SRC effects.

In these last years we have developed a model to describe the responses of finite nuclear systems within the framework of the correlated basis function theory. The model is inspired to the nuclear matter works of Refs. [7, 8]. With respect to these calculations, in our model the cluster expansion is truncated and only those terms containing a single correlation function are considered. The set of diagrams taken into account conserves the proper normalization of the many-body wave function.

We tested the validity of this treatment by comparing the nuclear matter charge responses calculated with our model with those obtained by the full expansion [9]. The excellent agreement between these two results gave us confidence in extending the application of the model to other cases. Since our description of the nuclear excitations does not treat properly collective states, we have selected situations dominated by single particle dynamics.

With our model we have studied the electromagnetic form factors of discrete states with large angular momentum [10]. These states are dominated by a single, or at most a few, particle-hole excitation. We found that the SRC produce small effects and are unable to account for the quenching required to reproduce the data. Electron scattering inclusive reactions in the quasi-elastic region have been investigated in [1]. In this case the effect of the correlations is much smaller than that produced by the final state interaction, and therefore difficult to disentangle. We have also investigated phenomena where a single nucleon is emitted by the interaction with a virtual [2] or real [3] photon. The study of (e,e'p) reactions show a very small sensitivity to the SRC. The dominant effect beyond the independent particle model is produced by the final state interaction. Nucleon emission induced by real photons shows a larger sensitivity to SRC, especially for excitation energies around 200 MeV and large nucleon emission angles [3]. Unfortunately, in this case, the meson exchange currents produce effects even larger than those induced by the SRC.

The difficulty in identifying clear SRC effects in our previous studies was due to the presence of the large contribution of the uncorrelated one-body responses that dominates the cross sections. A possibility of eliminating the one-body responses is offered by two-nucleon emission experiments. Only two-body transition operators can induce the emission of two nucleons. These operators can effectively be constructed by one-body operators acting on a correlated nucleonic pair, or by meson exchange currents. If the two emitted nucleons are of the same type, two protons for example, the meson exchange currents contributions produced by the exchange of a single charged mesons do not contribute. These facts make two-proton emission experiments an ideal tool to investigate SRC.

From the theoretical point of view, two-nucleon emission processes have been systematically studied in these years by the Pavia and Gent groups. The approach of the Pavia group [11, 12] is based on the two-nucleon spectral function, and, from the theoretical point of view, it is a straightforward extension of the well tested approach used to describe single nucleon emission processes. Recently two-nucleon spectral functions calculated with microscopic theories [13, 14] have been used. The Gent group [15]-

[17], calculates transition amplitudes produced by effective two-body operators that are formed by connecting the traditional one-body electromagnetic operators to two-nucleon correlation function.

The experimental situation is quite promising. After testing the feasibility of the experiment [18, 19], angular correlations of the cross sections have been measured [20, 21]. Other experiments of this kind have been planned.

In this article we present the results obtained by applying our model to the study of two-proton emission induced by electron scattering. A comparison of our results with the available data is out the scope of the present article. Our aim is to investigate the sensitivity of the (e,e'2p) cross section to the details of the SRC. To this purpose we have studied the influence on the cross section of the various theoretical inputs required by the calculation.

A summary of the basic formulae used to describe (e,e'2p) processes and electromagnetic currents is given in Section 2. In Section 3 we describe our nuclear model and in Section 4 we discuss the results we have obtained in ^{12}C , ^{16}O and ^{40}Ca target nuclei. In the last section we draw our conclusions.

2 THE CROSS SECTION

A detailed derivation of the cross section for double coincidence experiments can be found in [22]. In this section we briefly recall the expressions used in our calculations. We work in natural units ($\hbar = c = 1, e^2 = 1/137.04$) and employ the conventions of Bjorken and Drell [23]. The initial and final electron four-vectors are respectively $k \equiv (\epsilon, \mathbf{k})$ and $k' \equiv (\epsilon', \mathbf{k}')$, and $q \equiv (\omega, \mathbf{q}) = k - k'$ is the four-momentum transfer. The four-momenta of the emitted nucleons are indicated with $p_1 \equiv (\epsilon_1, \mathbf{p}_1)$ and $p_2 \equiv (\epsilon_2, \mathbf{p}_2)$.

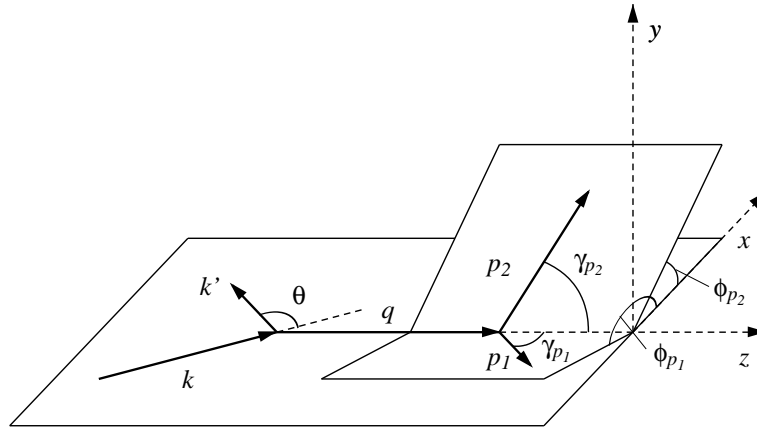


Figure 1: Reference system used in our calculations.

The reference system we adopt is shown in Fig. 1. The scattering plane is defined by the electron vectors \mathbf{k} and \mathbf{k}' , θ is the angle of the scattered electron and the quantization axis is taken along the direction of \mathbf{q} . The directions of the emitted nucleons are determined by the angles γ_{p_i} and ϕ_{p_i} , $i = 1, 2$. To simplify the formalism our calculations have been done considering two different angles φ_{p_i} and θ_{p_i} . The relation to the angles described in the figure is

$$\varphi_{p_i} = \begin{cases} \phi_{p_i} & \text{if } 0 \leq \phi_{p_i} \leq \pi \\ \phi_{p_i} - \pi & \text{if } \pi \leq \phi_{p_i} \leq 2\pi \end{cases} ,$$

and

$$\theta_{p_1} = \begin{cases} 2\pi - \gamma_{p_1} & \text{if } 0 \leq \gamma_{p_1} \leq \pi \\ \gamma_{p_1} & \text{if } \pi \leq \gamma_{p_1} \leq 2\pi \end{cases} ,$$

$$\theta_{p_2} = \begin{cases} \gamma_{p_2} & \text{if } 0 \leq \gamma_{p_2} \leq \pi \\ 2\pi - \gamma_{p_2} & \text{if } \pi \leq \gamma_{p_2} \leq 2\pi \end{cases} .$$

Note that the γ_{p_2} angle in Fig. 1 has been defined positive in the half plane containing the scattered electron. The convention for γ_{p_1} is opposite.

We have derived the cross section expression by considering that the electron wave functions are plane wave solutions of the Dirac equation. We suppose that only one photon is exchanged between the electron and the nucleus and we neglect all the terms depending on the electron rest mass. With these approximations we obtain

$$\frac{d^8\sigma}{d\epsilon'd\Omega_e d\epsilon_1 d\Omega_{p_1} d\Omega_{p_2}} = \frac{K}{(2\pi)^6} \sigma_{\text{Mott}} f_{\text{rec}} (v_l w_l + v_t w_t + v_{tl} w_{tl} + v_{tt} w_{tt}), \quad (1)$$

where we have indicated with σ_{Mott} the Mott cross section

$$\sigma_{\text{Mott}} = \left(\frac{e^2 \cos(\theta/2)}{2\epsilon \sin^2(\theta/2)} \right)^2, \quad (2)$$

and with f_{rec} the recoil factor

$$f_{\text{rec}}^{-1} = 1 + \frac{m}{M_{A-2}} \left[1 + \frac{|\mathbf{p}_1|}{|\mathbf{p}_2|} \cos \theta_{12} - \frac{|\mathbf{q}|}{|\mathbf{p}_2|} \cos \theta_{p_2} \right], \quad (3)$$

where θ_{12} is the angle between the momenta of the two emitted nucleons, \mathbf{p}_1 and \mathbf{p}_2 , and m and M_{A-2} are the nucleon and rest nucleus masses, respectively. The factor K is

$$K = m^2 |\mathbf{p}_1| |\mathbf{p}_2|, \quad (4)$$

because we used non relativistic kinematics to describe the motion of the two emitted nucleons. The expression (1) has been obtained by integrating on the energy ϵ_2 of one of the emitted particles and using the energy conservation.

In the plane wave approximation the leptonic and hadronic vertexes can be factorized. In our expression (1) the terms v come from the leptonic vertex and depend only from kinematic variables

$$v_l = \left(\frac{q_\mu^2}{\mathbf{q}^2} \right)^2, \quad (5)$$

$$v_t = \tan^2 \frac{\theta}{2} - \frac{1}{2} \frac{q_\mu^2}{\mathbf{q}^2}, \quad (6)$$

$$v_{tl} = \frac{q_\mu^2}{\sqrt{2}\mathbf{q}^2} \left(\tan^2 \frac{\theta}{2} - \frac{q_\mu^2}{\mathbf{q}^2} \right)^{\frac{1}{2}}, \quad (7)$$

$$v_{tt} = \frac{1}{2} \frac{q_\mu^2}{\mathbf{q}^2}. \quad (8)$$

The information about the nuclear structure is included in the w factors. Because of the current conservation only three components of the four-vector current are independent. We choose the charge $\rho(\mathbf{q})$ and the two transverse components in spherical coordinates

$$J_\pm = \mp \frac{1}{\sqrt{2}} (J_x \pm iJ_y). \quad (9)$$

In analogy to the (e,e'p) case [2] the w factors can be expressed as

$$w_l = \langle \Psi_i | \rho^\dagger(\mathbf{q}) | \Psi_f \rangle \langle \Psi_f | \rho(\mathbf{q}) | \Psi_i \rangle, \quad (10)$$

$$w_t = \langle \Psi_i | J_-^\dagger(\mathbf{q}) | \Psi_f \rangle \langle \Psi_f | J_-(\mathbf{q}) | \Psi_i \rangle + \langle \Psi_i | J_+^\dagger(\mathbf{q}) | \Psi_f \rangle \langle \Psi_f | J_+(\mathbf{q}) | \Psi_i \rangle, \quad (11)$$

$$w_{tl} = 2\text{Re} \left(\langle \Psi_i | \rho^\dagger(\mathbf{q}) | \Psi_f \rangle \langle \Psi_f | J_-(\mathbf{q}) | \Psi_i \rangle - \langle \Psi_i | \rho^\dagger(\mathbf{q}) | \Psi_f \rangle \langle \Psi_f | J_+(\mathbf{q}) | \Psi_i \rangle \right), \quad (12)$$

$$w_{tt} = 2\text{Re} \left(\langle \Psi_i | J_+^\dagger(\mathbf{q}) | \Psi_f \rangle \langle \Psi_f | J_-(\mathbf{q}) | \Psi_i \rangle \right), \quad (13)$$

where we have indicated with $|\Psi_i\rangle$ and $|\Psi_f\rangle$ the initial and final states of the full hadronic system. We do not consider the polarization of the emitted nucleons, therefore, in the previous equations, a sum on the third components of the spin of the emitted particles and of the angular momentum of the residual nucleus is understood.

The one-body electromagnetic operators we have used are produced by the charge operator

$$\rho(\mathbf{r}) = \sum_{k=1}^A \frac{1 + \tau_3(k)}{2} \delta(\mathbf{r} - \mathbf{r}_k), \quad (14)$$

and by the magnetization current operator

$$J^M(\mathbf{r}) = \sum_{k=1}^A \frac{1}{2m_k} \left(\mu^P \frac{1 + \tau_3(k)}{2} + \mu^N \frac{1 - \tau_3(k)}{2} \right) \nabla \times \delta(\mathbf{r} - \mathbf{r}_k) \boldsymbol{\sigma}(k). \quad (15)$$

In the previous equations m_k indicates the rest mass of k -th nucleon, μ^P and μ^N the anomalous magnetic moment of the proton and the neutron, respectively, $\boldsymbol{\sigma}(k)$ the Pauli spin matrix of the k -th nucleon and $\tau_3(k) = 1$ (-1) if the k -th nucleon is a proton (neutron). In our calculations the nucleonic internal structure has been considered by folding the point-like responses with the electromagnetic nucleon form factors of Ref. [24]. To simplify the calculations we did not include the convection current because we know that its contribution is small in the quasi-elastic region [1, 3].

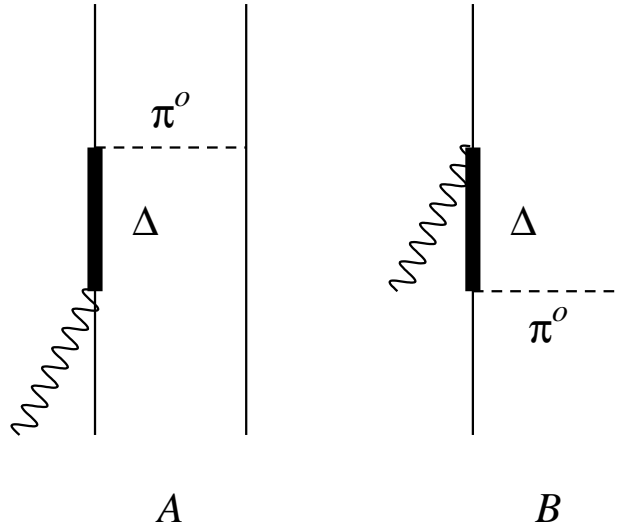


Figure 2: Meson exchange currents diagrams considered in our calculations. The wiggly lines represent the virtual photon exchanged with the electron, the full thin lines the nucleons. Since we describe the emission of two protons, the exchanged pion is chargeless.

Since we have considered only the emission of two like particles (two protons), the two-body currents induced by the exchange of charged mesons do not contribute. The main two-body current contribution arises from diagrams like those of Fig. 2 where the exchanged π meson is chargeless. These diagrams correspond to the Δ -isobar currents for which we have used the following expression

$$\begin{aligned} \mathbf{j}^\Delta(\mathbf{r}) = & \frac{f_{\pi N\Delta} f_{\pi NN} f_{\gamma N\Delta}}{9m_\pi^3} \sum_{k < l = 1}^A \tau_3(l) \nabla \times \delta(\mathbf{r} - \mathbf{r}_k) \\ & \left[i 2 G_\Delta^- \boldsymbol{\sigma}(l) \times \nabla - 4 G_\Delta^+ \nabla \right] \left[\boldsymbol{\sigma}(k) \cdot \nabla \mathcal{H}(\mathbf{r} - \mathbf{r}_l, \varepsilon_l) \right] \\ & + (k \longleftrightarrow l), \end{aligned} \quad (16)$$

where the factors $f_{\pi N\Delta}$, $f_{\pi NN}$ and $f_{\gamma N\Delta}$ are the coupling constants related to the processes indicated by the lower labels, and m_π is the pion mass. The Fourier transform of the above expression has been

multiplied by the Δ electromagnetic form factor F_Δ that we have considered in its dipole form

$$F_\Delta(|\mathbf{q}|, \omega) = \left[1 - \frac{\omega^2 - \mathbf{q}^2}{\Lambda^2} \right]^{-2}, \quad (17)$$

with $\Lambda=855$ MeV when ω and \mathbf{q} are expressed in MeV. The two coupling constants G_Δ^+ and G_Δ^- are related to the two diagrams shown in Fig. 2 and are defined as

$$G_\Delta^\pm = G_A \pm G_B, \quad (18)$$

Following the indications of Refs. [25, 26], we have taken the coupling

$$G_A = \left[m_\Delta - \sqrt{s} - \frac{i}{2} \Gamma_\Delta(\sqrt{s}) \right]^{-1}, \quad (19)$$

where

$$s = 2\omega(m_n + \epsilon_h) + (m_n + \epsilon_h)^2, \quad (20)$$

and ϵ_h is energy of the hole single particle level. The expression of the imaginary part is taken from Ref. [27],

$$\Gamma_\Delta(\sqrt{s}) = \frac{8 f_{\pi NN} (m_\Delta - m_n) (s - m_\pi^2)^{3/2}}{3 m_\pi^2 \sqrt{s}}. \quad (21)$$

On the other hand,

$$G_B = (m_\Delta - m_n)^{-1}. \quad (22)$$

In the previous equations $m_\Delta = 1232$ MeV and $m_n = 938.9$ MeV are the Δ and nucleon masses, respectively. Finally, with the function $\mathcal{H}(\mathbf{r})$ we indicated the Fourier transform of the dynamical pion propagator

$$\mathcal{H}(\mathbf{r} - \mathbf{r}_l, \varepsilon_l) = \int \frac{d^3k}{(2\pi)^3} \frac{F_{\pi N}(k, \varepsilon_l) e^{i\mathbf{k}\cdot(\mathbf{r}-\mathbf{r}_l)}}{k^2 + m_\pi^2 - \varepsilon_l^2}, \quad (23)$$

where $F_{\pi N}$ is the pion-nucleon form factor and ε_l is the energy of the exchanged pion obtained as the difference between the energies of the final and initial states of the l -th nucleon. To simplify our calculations we set the pion-nucleon form factor $F_{\pi N}(k, \varepsilon) = 1$. We have verified that it is a very good assumption in the energy and momentum region we are interested to explore [28].

3 THE NUCLEAR MODEL

In the previous section we have presented the expressions of the cross sections and of the electromagnetic operators used in our calculations. Now we have to specify how we describe the initial and final nuclear states to be used to calculate the transition matrix elements in Eqs. (10)-(13). To simplify the presentation we will be first concerned with the description of the final state which, asymptotically, has two nucleons in the continuum and two holes. In a following step we shall discuss how we describe the correlated many-body states. Our numerical calculations have been restricted to the case of the emission of two protons, but the formalism is general enough to deal with the emission of two generic nucleons.

We describe the single particle wave function of a nucleon moving in the continuum with momentum \mathbf{p} and with third components of spin and isospin s and t , respectively, as

$$\psi(\mathbf{p} \cdot \mathbf{r}) \chi_s \chi_t = \frac{4\pi}{|\mathbf{p}|} \sum_{l=0}^{\infty} \sum_{\mu=-l}^l \sum_{j=l\pm 1/2} (-i)^l R_{l,j}^t(pr) Y_{l\mu}^*(\Omega_p) \langle l\mu \frac{1}{2} s | jm \rangle Y_{l,j}^m(\Omega_r) \chi_t. \quad (24)$$

In the above equation we have done the multipole decomposition of the wave function and we have indicated with $\langle l\mu \frac{1}{2} s | jm \rangle$ the Clebsch-Gordan coefficients, with $Y_{l\mu}$ the spherical harmonics and with

$$Y_{l,j}^m(\Omega) = \sum_{\mu s} \langle l\mu \frac{1}{2} s | jm \rangle Y_{l\mu}(\Omega) \chi_s \equiv |l \frac{1}{2} j m\rangle, \quad (25)$$

the spin spherical harmonics [29]. The symbols χ_s and χ_t indicate, respectively, the spin and isospin parts of the wave function and $R_{l,j}^t(pr)$ its radial part, obtained by solving the Schrödinger equation with a spherical mean field potential.

The many-body final state is characterized by the momenta of the emitted nucleons \mathbf{p}_1 and \mathbf{p}_2 , their spin and isospin components s_1, s_2, t_1 and t_2 , the total angular momentum of the residual nucleus J_h and its z-axis component M_h , and the orbital and total angular momenta, $l_{h_1}, j_{h_1}, l_{h_2}$ and j_{h_2} , of the single particle states where the nucleons are coming from

$$|\Psi_f(\mathbf{p}_1, s_1, t_1, \mathbf{p}_2, s_2, t_2; J_h, M_h; l_{h_1}, j_{h_1}, l_{h_2}, j_{h_2})\rangle = a_{p_1 s_1}^+ a_{p_2 s_2}^+ \left[\tilde{a}_{l_{h_1}, j_{h_1}} \otimes \tilde{a}_{l_{h_2}, j_{h_2}} \right]_{M_h}^{J_h} |\Psi(0, 0)\rangle. \quad (26)$$

In the above equation a_{ps}^+ creates a particle with momentum $|\mathbf{p}|$ and spin third component s (the isospin indexes have been dropped to simplify the writing), and we have defined the annihilation operator as

$$\tilde{a}_{l,j,m} = (-1)^{j+m} a_{l,j,-m}, \quad (27)$$

in order to deal with irreducible spherical tensors. The symbol \otimes indicates the tensor product between two of such tensors [29].

The nuclear ground state is represented by $|\Psi(0, 0)\rangle$ defined as

$$|\Psi(0, 0)\rangle = \frac{F|\Phi(0, 0)\rangle}{\langle\Phi(0, 0)|F^+F|\Phi(0, 0)\rangle}, \quad (28)$$

where F is the correlation function and $|\Phi(0, 0)\rangle$ is the Slater determinant describing a mean field ground state. We work with doubly magic nuclei, therefore the two zeros on the ground state symbol indicate the angular momentum value and its projection on the quantization axis.

By considering the multipole expansion of the single particle continuum wave function we can write

$$\begin{aligned} & |\Psi_f(\mathbf{p}_1, s_1, t_1, \mathbf{p}_2, s_2, t_2; J_h, M_h; l_{h_1}, j_{h_1}, l_{h_2}, j_{h_2})\rangle \\ &= \frac{(4\pi)^2}{|\mathbf{p}_1| |\mathbf{p}_2|} \sum_{l_{p_1} \mu_{p_1}} \sum_{j_{p_1} m_{p_1}} \sum_{l_{p_2} \mu_{p_2}} \sum_{j_{p_2} m_{p_2}} (-i)^{l_{p_1} + l_{p_2}} \\ & Y_{l_{p_1} m_{p_1}}(\Omega_{p_1}) Y_{l_{p_2} m_{p_2}}(\Omega_{p_2}) \langle l_{p_1} \mu_{p_1} \frac{1}{2} s_1 | j_{p_1} m_{p_1} \rangle \langle l_{p_2} \mu_{p_2} \frac{1}{2} s_2 | j_{p_2} m_{p_2} \rangle \\ & |\Psi_f(l_{p_1}, \mu_{p_1}, j_{p_1}, m_{p_1}; l_{p_2}, \mu_{p_2}, j_{p_2}, m_{p_2}; l_{h_1}, j_{h_1}; l_{h_2}, j_{h_2}; J_h, M_h)\rangle. \quad (29) \end{aligned}$$

The many-body final state on the right hand side of the above equation is described as

$$\begin{aligned} & |\Psi_f(l_{p_1}, \mu_{p_1}, j_{p_1}, m_{p_1}; l_{p_2}, \mu_{p_2}, j_{p_2}, m_{p_2}; l_{h_1}, j_{h_1}; l_{h_2}, j_{h_2}; J_h, M_h)\rangle \\ &= \sum_{m_{h_1} m_{h_2}} (-1)^{j_{h_1} + m_{h_1} + j_{h_2} + m_{h_2}} \langle j_{h_1} - m_{h_1} j_{h_2} - m_{h_2} | J_h M_h \rangle \frac{F|\Phi_f\rangle}{\langle\Phi_f|F^+F|\Phi_f\rangle^{\frac{1}{2}}} \quad (30) \end{aligned}$$

The Slater determinant $|\Phi_f\rangle$ is built on the ground state Slater determinant $|\Phi(0, 0)\rangle$ by substituting the hole wave functions h_1 and h_2 with the particle wave functions p_1 and p_2 . In this specific case, the various single particle wave functions are not coupled to a total angular momentum, therefore the quantum numbers characterizing $|\Phi_f\rangle$ are the orbital, l , and total, j , angular momenta of the single particle levels, their z-axis projections, μ and m , respectively, and the third components of the isospin.

The evaluation of the w functions in Eqs. (10)-(13) requires the calculation of transition matrix elements of the type

$$\begin{aligned} \langle\Psi_f|O_\eta(\mathbf{q})|\Psi(0, 0)\rangle &= \frac{(4\pi)^2}{|\mathbf{p}_1| |\mathbf{p}_2|} \sum_{l_{p_1} \mu_{p_1}} \sum_{j_{p_1} m_{p_1}} \sum_{l_{p_2} \mu_{p_2}} \sum_{j_{p_2} m_{p_2}} \sum_{m_{h_1} m_{h_2}} i^{l_{p_1} + l_{p_2}} (-1)^{j_{h_1} + m_{h_1} + j_{h_2} + m_{h_2}} \\ & \langle l_{p_1} \mu_{p_1} \frac{1}{2} s_1 | j_{p_1} m_{p_1} \rangle \langle l_{p_2} \mu_{p_2} \frac{1}{2} s_2 | j_{p_2} m_{p_2} \rangle \langle j_{h_1} - m_{h_1} j_{h_2} - m_{h_2} | J_h M_h \rangle \\ & Y_{l_{p_1} m_{p_1}}^*(\Omega_{p_1}) Y_{l_{p_2} m_{p_2}}^*(\Omega_{p_2}) \xi[O_\eta(\mathbf{q}) : p_1, p_2, h_1, h_2], \quad (31) \end{aligned}$$

where

$$O_\eta(\mathbf{q}) = \int d^3r e^{-i\mathbf{q}\cdot\mathbf{r}} O_\eta(\mathbf{r}), \quad (32)$$

indicates a one-body electromagnetic operator and we have defined

$$\begin{aligned} \xi[O_\eta(\mathbf{q}) : p_1, p_2, h_1, h_2] &= \frac{\langle \Phi_f | F^+ O_\eta(\mathbf{q}) F | \Phi(0, 0) \rangle}{\langle \Phi_f | F^+ F | \Phi_f \rangle^{\frac{1}{2}} \langle \Phi(0, 0) | F^+ F | \Phi(0, 0) \rangle^{\frac{1}{2}}} \\ &= \frac{\langle \Phi_f | F^+ O_\eta(\mathbf{q}) F | \Phi(0, 0) \rangle}{\langle \Phi_f | F^+ F | \Phi_f \rangle} \left[\frac{\langle \Phi_f | F^+ F | \Phi_f \rangle}{\langle \Phi(0, 0) | F^+ F | \Phi(0, 0) \rangle} \right]^{\frac{1}{2}}. \end{aligned} \quad (33)$$

In our calculations we have used purely scalar correlations defined as:

$$F(1, 2, \dots, A) = \prod_{i < j}^A f(r_{ij}), \quad (34)$$

where $r_{ij} = |\mathbf{r}_i - \mathbf{r}_j|$ is the distance between the positions of the particles i and j .

The two factors in Eq. (33) are separately evaluated by expanding numerator and denominator in powers of the two-body short-range correlation function f . The presence of the denominator and the energy conservation eliminate the unlinked diagrams.

Since in our calculations the correlation functions are purely scalar they commute with the operator $O_\eta(\mathbf{q})$ therefore:

$$\begin{aligned} \xi[O_\eta(\mathbf{q}) : p_1, p_2, h_1, h_2] &= \langle \Phi; p_1, p_2, h_1, h_2 | O_\eta(\mathbf{q}) F^2 | \Phi; 00, +1 \rangle_L \\ &= \langle \Phi; p_1, p_2, h_1, h_2 | O_\eta(\mathbf{q}) \prod_{i < j}^A (1 + h_{ij}) | \Phi(0, 0) \rangle_L, \end{aligned} \quad (35)$$

where we have used the function $h_{ij} = f^2(r_{ij}) - 1$ and the subindex L indicates that only the linked diagrams are considered.

The approximation of our model consists in retaining only those terms where the h_{ij} function appears only once

$$\begin{aligned} \xi[O_\eta(\mathbf{q}) : p_1, p_2, h_1, h_2] &\longrightarrow \xi^1[O_\eta(\mathbf{q}) : p_1, p_2, h_1, h_2] \\ &= \langle \Phi; p_1, p_2, h_1, h_2 | O_\eta(\mathbf{q}) (1 + \sum_{i < j} h_{ij}) | \Phi(0, 0) \rangle_L \\ &= \langle \Phi; p_1, p_2, h_1, h_2 | O_\eta(\mathbf{q}) \sum_{1 < j} h(r_{1,j}) | \Phi(0, 0) \rangle_L \\ &\quad + \langle \Phi; p_1, p_2, h_1, h_2 | O_\eta(\mathbf{q}) \sum_{1 < i < j} h(r_{i,j}) | \Phi(0, 0) \rangle_L. \end{aligned} \quad (36)$$

This result has been obtained using a procedure analogous to that adopted in Ref. [30] for the evaluation of the density distribution, therefore the truncation of the expansion is done only after the elimination of the unlinked diagrams. The Meyer-like diagrams considered in our work are presented in Fig. 3. It is evident that, in this case, the uncorrelated term, produced by the 1 in Eq. (36), does not contribute. All the terms necessary to calculate the cross section have been specified. The detailed calculation of the various matrix elements for the one-body current is presented in the Appendix A.

The Δ currents allow for the two-nucleon emission already at the independent particle model level. We consider only this contribution, therefore SRC and Δ currents are not directly coupled in our model. They influence each other only via the interference terms.

4 SPECIFIC APPLICATIONS

The interest in studying two-nucleon emission cross sections, is related to the possibility of obtaining information on the SRC. In order to identify correlation effects it is necessary to keep under control

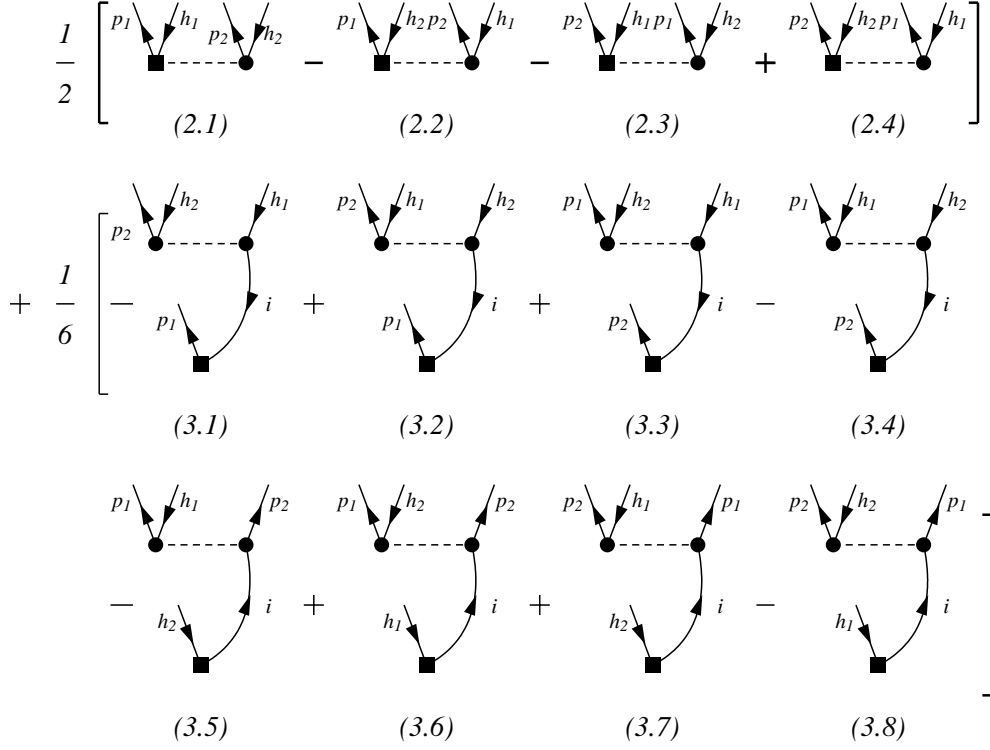


Figure 3: Meyer-like diagrams representing the one-body currents matrix elements included in our calculations. The dashed lines represent the function $h(r) = f^2(r) - 1$, where $f(r)$ is the correlation function. The black squares are the points where the electromagnetic one-body operator $\mathcal{O}_\eta(\mathbf{r})$ is acting. The oriented full lines represent single particle wave functions and one has to understand a sum on all the hole states labeled with i .

all the other variables which can affect the cross section. For this reason, before studying the influence of the SRC we shall discuss the sensitivity of the cross section to the various theoretical inputs of our model. The results of this investigation will be presented only for the reaction $^{16}\text{O}(e,e'2p)^{14}\text{C}$, but we have done calculations also for ^{12}C and ^{40}Ca nuclei. The two-hole composition of the various final states we have considered is given in Table 1.

	^{12}C	^{16}O	^{40}Ca
0_1^+	$(1p3/2)^{-2}$	$(1p1/2)^{-2}$	$(1d3/2)^{-2}$
0_2^+		$(1p3/2)^{-2}$	$(2s1/2)^{-2}$
1^+		$(1p1/2)^{-1} (1p3/2)^{-1}$	$(1d3/2)^{-1} (2s1/2)^{-1}$
2_1^+	$(1p3/2)^{-2}$	$(1p1/2)^{-1} (1p3/2)^{-1}$	$(1d3/2)^{-2}$
2_2^+		$(1p3/2)^{-2}$	$(1d3/2)^{-1} (2s1/2)^{-1}$

Table 1: Two-hole compositions of the final states considered in our study.

4.1 Kinematics and No-Recoil Approximation

The definition of the kinematics of the reaction under investigation is far from being trivial. Energy and momentum conservation imply

$$\omega = \epsilon_1 + \epsilon_2 - \epsilon_{h_1} - \epsilon_{h_2} + \frac{\mathbf{p}_r^2}{2M_{A-2}}, \quad (38)$$

$$\mathbf{q} = \mathbf{p}_1 + \mathbf{p}_2 + \mathbf{p}_r, \quad (39)$$

where we have considered non relativistic kinematics and we have indicated with \mathbf{p}_r the recoil momentum of the $A - 2$ residual nucleus. The other symbols have been already defined in the previous sections.

In our calculations we fixed ω , \mathbf{q} , and \mathbf{p}_2 . By selecting the $A - 2$ nucleus final state also ϵ_{h_1} and ϵ_{h_2} are fixed. The cross sections are presented as a function of γ_{p_1} . By solving the above system of equations we obtain the values of $|\mathbf{p}_r|$ and $|\mathbf{p}_1|$ for each γ_{p_1} . This means that in the calculation of the nuclear transition matrix elements, the radial integrals shown in Appendix A, should be calculated for each value of γ_{p_1} . From the computational point of view, the situation improves enormously by assuming $\mathbf{p}_r = 0$, since in this case $|\mathbf{p}_1|$ becomes independent from γ_{p_1} . We call No-Recoil Approximation (NRA) this approximation, consisting in setting to zero the kinetic energy and the momentum of the residual $A - 2$ nucleus.

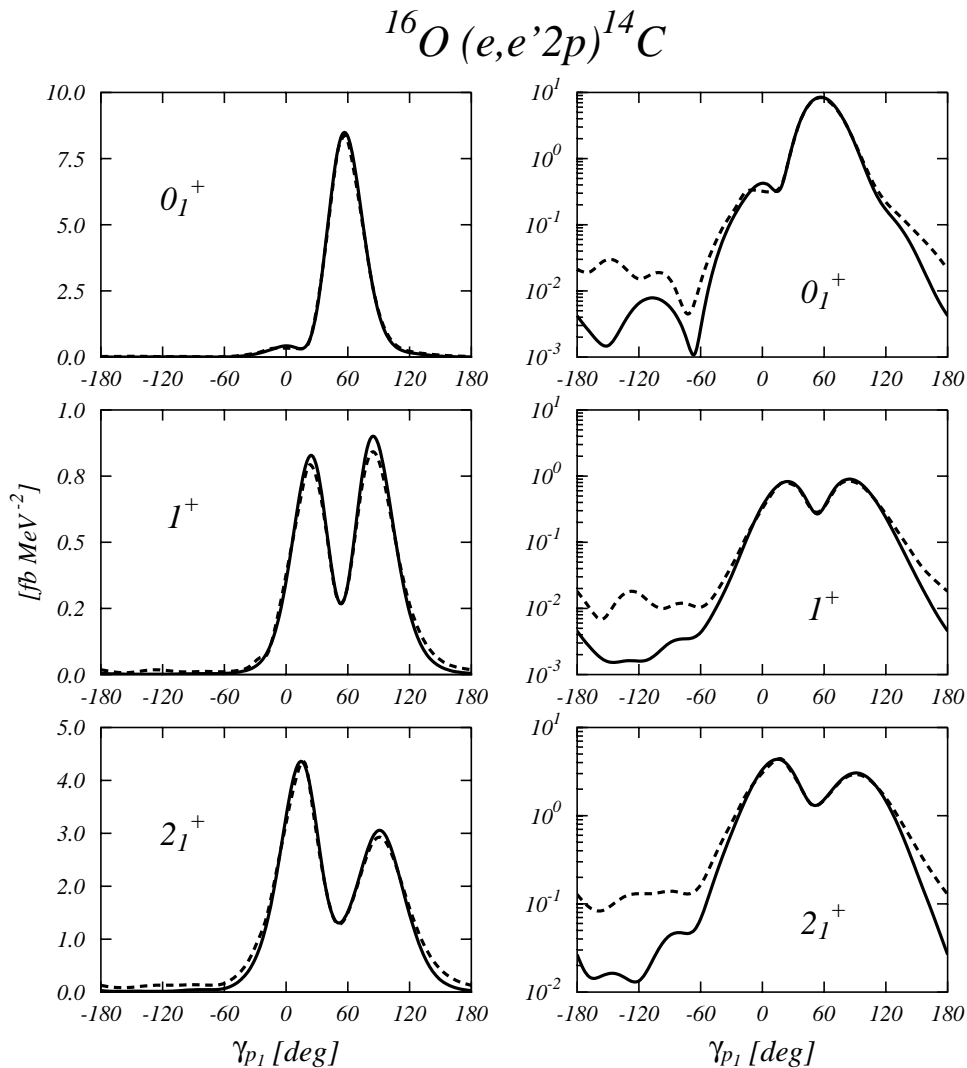


Figure 4: Cross sections for the $^{16}\text{O}(e,e'2p)^{14}\text{C}$ reaction in the *standard kinematics* (see Sect. 4.2). The two-hole composition of the final states is given in Table 1. The dashed lines have been obtained by properly considering the recoil energy of the ^{14}C nucleus. The full lines have been obtained within the NRA. The left and right panels show the same results in linear and logarithmic scale.

In Fig. 4 we compare the results of the NRA (full lines) with those obtained by correctly treating the $A - 2$ nucleus recoil (dashed lines). The reaction is $^{16}\text{O}(e,e'2p)^{14}\text{C}$ and the calculations have been done in what we shall define in Sect. 4.2 as *standard kinematics*. The left and right panels show the same results in linear and logarithmic scale. This presentation is done to show that the two results are very similar in the peak region. The differences are relevant only off the maximum region, but

they can be appreciated only in logarithmic scale since in that region the cross section values fall by several order of magnitude with respect to the peak values.

We have verified that, in the kinematics used in the calculations, the recoil factor in Eq. (3) differs from 1 at most by a 4%. Therefore the source of the difference is related to the change of the single particle wave functions because of the change of $\epsilon_1 = \mathbf{p}_1^2/2m$. In the kinematics under investigation this energy can vary from 34.0 down to 22.6 MeV. It is interesting to notice that, in the region where the cross section has its maximum, or maxima, the results of the two calculations are rather similar. This feature can be more easily understood by considering the emitted nucleon wave functions as plane waves. In this case by using Eq. (32) one can observe that the calculation of the matrix element (35) is related to the Fourier transform of the two-hole relative wave functions with respect to the variable $\mathbf{p}_r = \mathbf{q} - (\mathbf{p}_1 + \mathbf{p}_2)$. As it has been pointed out in Refs. [12, 16, 17], the maximum value of this transform occurs when the argument has its minimum value, possibly zero. For this reason the results of the two calculations shown in Fig. 4 are rather similar in the region of the maxima.

The good performances of the NRA, at least in the region where the cross section shows its maxima, gave us confidence about its use in our calculations. All the results presented in the following sections have been obtained in NRA.

4.2 The mean field

In this section we present the results of our study on the influence of the mean field used to generate the single particle wave functions on the (e,e'2p) cross sections. The investigation has been conducted on ^{16}O by fixing the correlation function and changing the mean field.

As in the case of our previous works on (e,e'p) and (γ ,p) reactions [2, 3], we used a real potential to generate the hole wave functions, and an optical potential to generate the particle wave functions. With this choice the single particle wave functions are not any more orthonormal. In our previous investigations [2, 3] we have studied these non-orthogonality effects, and we reached the same conclusions obtained in Ref. [31] where the problem has been first studied: for the case under investigation and the kinematics we intend to explore, these effects are negligible.

The parameters of the Woods-Saxon well used to generate the hole wave functions are those given in Ref. [32]. Associated to these single particle wave functions there are SRC obtained by minimizing the nuclear hamiltonian with the semi-realistic *S3* interaction of Afnan and Tang [33]. For our test cases we used the gaussian form of the correlation function taken from [32]:

$$f(r) = 1 - a e^{-br^2}, \quad (40)$$

with $a=0.7$ and $b=2.2 \text{ fm}^{-2}$. The particle wave functions have been obtained by using the optical potential of Schwandt *et al.* [34]. If not explicitly stated otherwise, these are the parameters used in our calculations.

Since the number of variables is quite large we have chosen specific kinematics to perform our test calculations. These kinematics, we call them *standard kinematics*, consist in fixing the electron incoming energy $\epsilon = 800 \text{ MeV}$ and the excitation energy $\omega = 100 \text{ MeV}$. Then we fixed $\epsilon_2 = 40 \text{ MeV}$ and the emission angle $\gamma_{p_2} = 60^\circ$. The energy of the other proton is obtained from Eq. (38) by setting $\mathbf{p}_r = 0$, that is in the NRA, and the cross section are presented as a function of γ_{p_1} , the emission angle. We always work in coplanar kinematics, i.e. ϕ_{p_1} and ϕ_{p_2} are zero. We recall that we have taken the angle γ_{p_1} to be positive on the opposite side of the scattered electron with respect to \mathbf{q} , while γ_{p_2} is taken positive on the same side of the scattered electron. We used this *standard kinematics* in ^{16}O as a reference calculation.

A first test has been done on the sensitivity of the results to the changes of the hole wave functions. An example of the results we have obtained is shown in Fig. 5. The standard results are shown by the full lines. The dashed lines have been obtained with the hole wave functions generated by the Woods-Saxon potential whose parameters are given in Table V of Ref. [35]. These parameters have been used in a Fermi hypernetted chain calculation done with the Argonne *V8'* nucleon-nucleon interaction. In this case the spin orbit term of the mean-field potential has been set to zero. The dotted lines have

$^{16}\text{O} (e, e' 2p) ^{14}\text{C}$

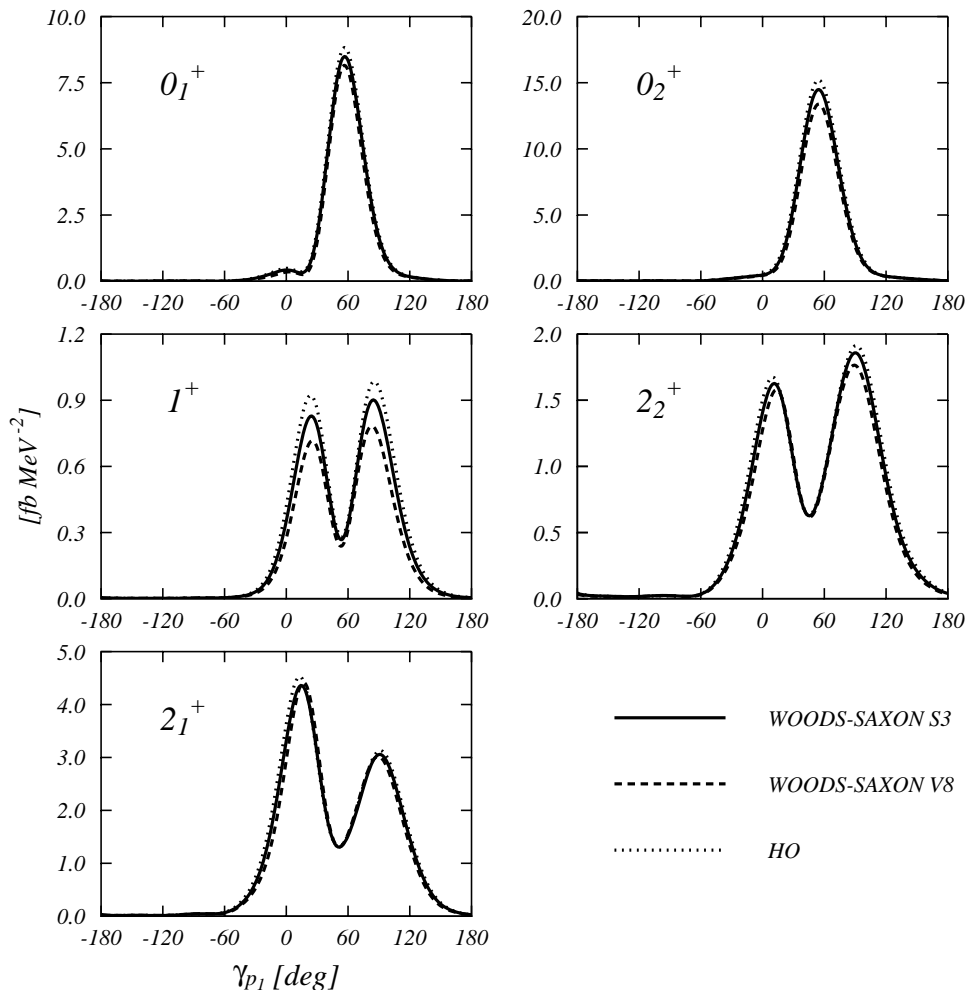


Figure 5: Cross sections calculated in *standard kinematics* with different mean field potentials generating the hole wave functions. The full lines show the standard results obtained by using the mean-field potential of Ref. [32]. The dashed lines have been obtained with the mean field potential of Ref. [35]. The dotted lines are results obtained with harmonic oscillator wave functions.

been obtained by using harmonic oscillator single particle wave functions. The sensitivity of various results to these changes is limited: we found a maximum variation of 4%, except for the case of the 1^+ state. This state is, however, out of the systematics, since it is dominated by the Δ currents, as we shall discuss in more detail in Sect. 4.3.

We should remark that all the mean-field potentials used in these test calculations reproduce the root mean square charge radii. Furthermore, the single particle energies have been kept constant in all the calculations. In our calculations, the hole single particle energies are used to determine the particle energies, see Eq. (38). The particle wave functions are calculated by solving the single particle Schrödinger equation with an energy dependent optical potential for a continuum wave. Changes in the energy of the particle could strongly modify the single particle hamiltonian, then the particle wave functions.

In our *standard kinematics* calculations we used the hole energies obtained by solving the single particle Schrödinger equation with the ground state Woods-Saxon potential. In the cases of our interest these single particle energies are given in Table 2. In this approach we do not consider the fact that a residual nucleon-nucleon interaction rearranges the mean field in the $A - 2$ nucleon system such that its energy is not any more the energy of the A nucleon system minus the two single particle energies. A way to take into account this fact is to use the experimental binding energies of the $A - 2$ nucleus, the ^{14}C in the specific case, and the energies of the first excited states which should be interpreted in

	1d5/2	2s1/2	1p1/2	1p3/2
^{12}C				-18.0
^{16}O			-12.7	-16.9
^{40}Ca	-8.7	-19.3		

Table 2: Single particle energies, in MeV, for the states of interest in our calculations. These energies have been obtained using the Woods-Saxon parameterization given in [32].

terms of single particle excitations. This is the approach used by Giusti and Pacati [12].

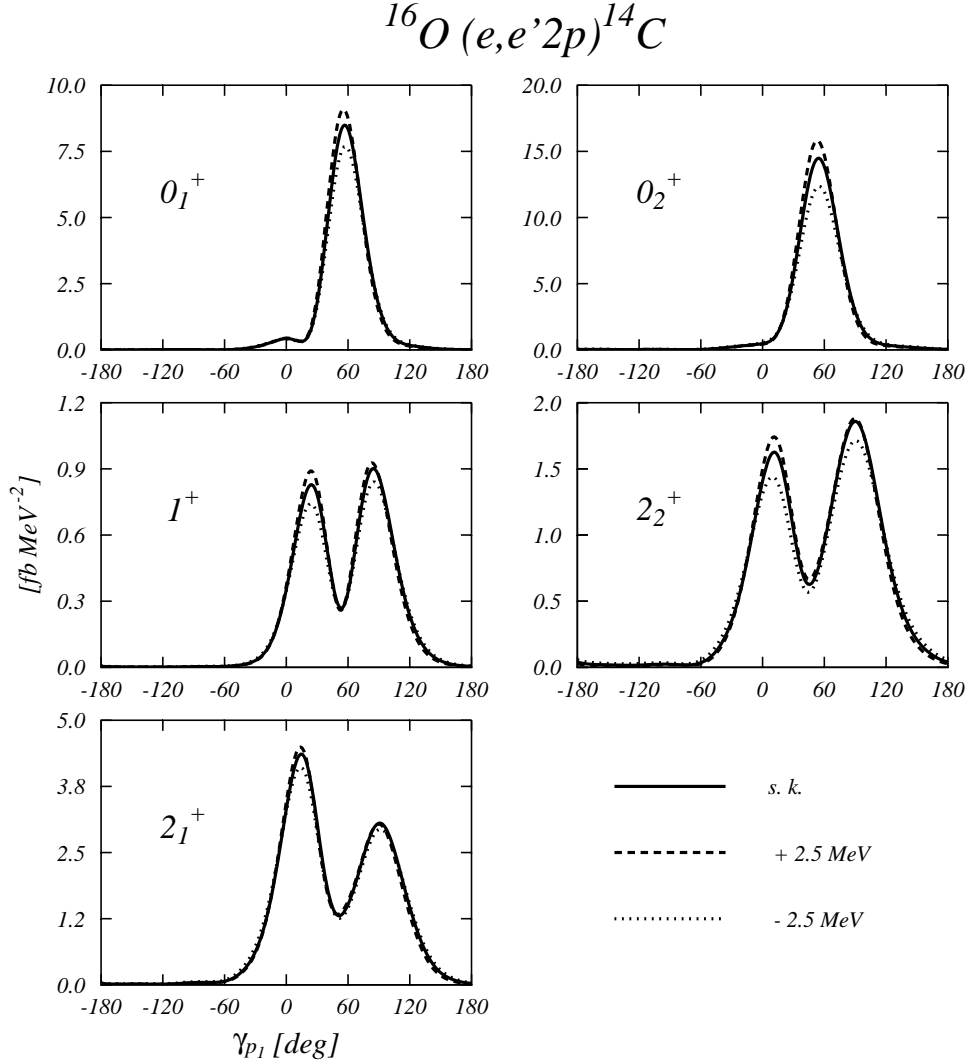


Figure 6: Comparison between cross sections calculated in *standard kinematics* (full lines) and those obtained by increasing (dashed lines) and reducing (dotted lines) ϵ_1 by 2.5 MeV.

From the pragmatic point of view the two methods of determining the hole single particle energies introduce an uncertainty of about 2.5 MeV. This uncertainty is reflected on the energies of the emitted particle and on their wave functions. The final uncertainties are shown in Fig. 6 where the results of the *standard calculations* are compared with those obtained by increasing and lowering ϵ_1 by 2.5 MeV.

The larger variation of the cross section obtained in Fig. 6 with respect to those of Fig. 5 indicates the great sensitivity of the results to the particle wave functions. In Fig. 7 we compare the results of the *standard calculation* with those obtained by using plane waves for the particle wave functions

(dotted lines) and with those obtained by using the same real Woods-Saxon potential utilized to describe the hole states (dashed lines). It is evident the large difference between the various results and it appears clear the effect of the complex optical potential whose imaginary part quenches the cross section.

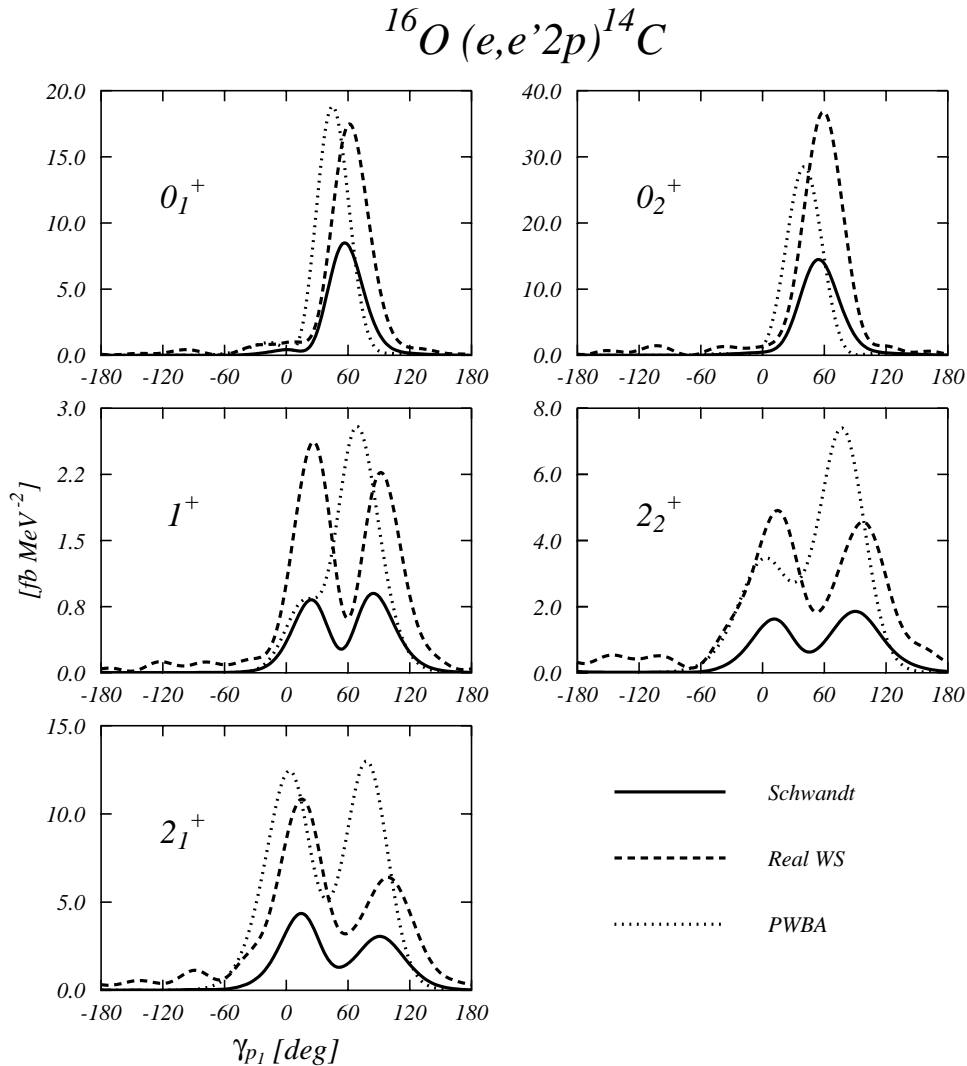


Figure 7: Cross sections calculated in *standard kinematics*. The standard results (full lines) are compared with those obtained by using plane waves (dotted lines) and real Woods-Saxon single particle wave functions (dashed lines).

The sensitivity of our calculations to the choice of the optical potential is shown in Fig. 8 where the cross sections have been calculated by using the optical potentials of Schwandt *et al.* [34] (the *standard calculations*), Nadasen *et al.* [36] and Comfort and Karp [37]. Though the modifications of the cross section are less pronounced than in Fig. 7, they can become as large as 18%.

We can conclude this section by saying that the various plausible choices of the mean-field parameters can produce uncertainties of about 20% - 30% on the maxima of the cross sections.

4.3 The two-body current

We have already pointed out that the presence of SRC is not the only mechanism inducing the emission of two protons. Meson exchange currents of the type shown in Fig. 2 can also contribute to this process. For the purpose of studying SRC the presence of these two-body currents is disturbing, therefore, it is important to find kinematics where the Δ currents contributions are negligible with

$^{16}\text{O} (e, e' 2p) ^{14}\text{C}$

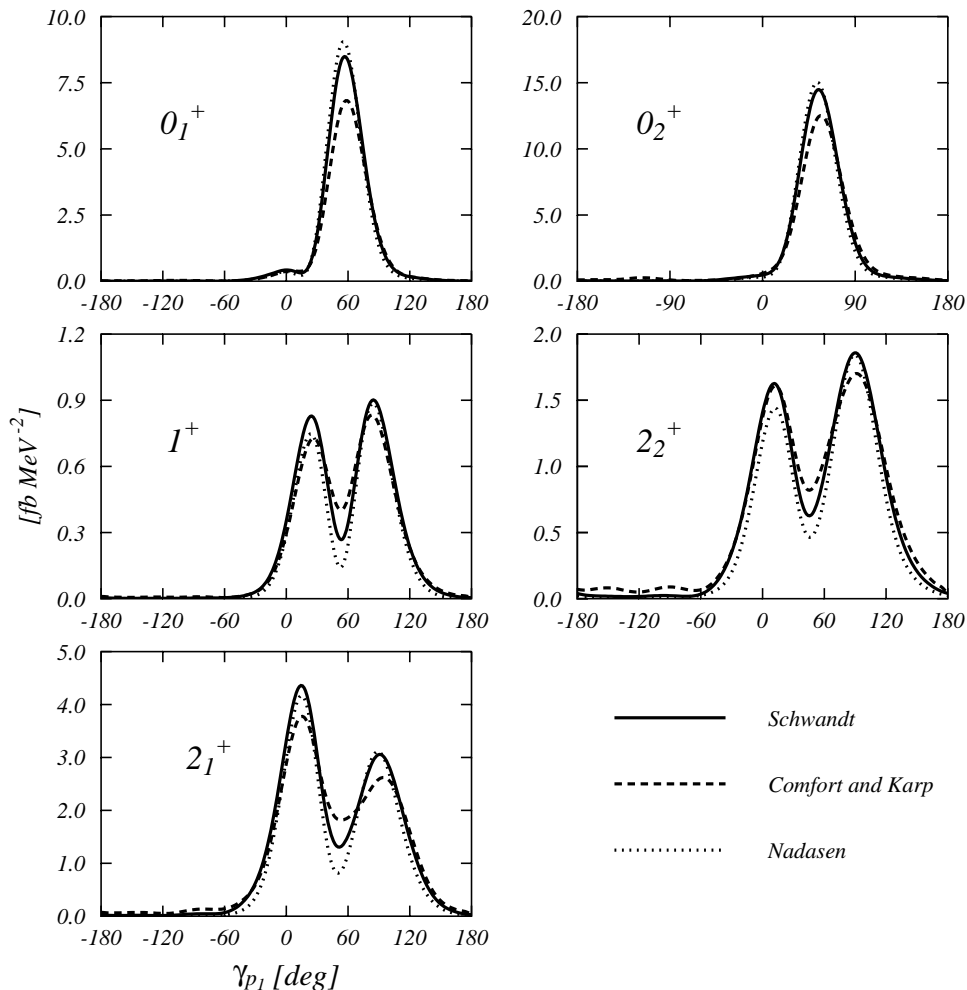


Figure 8: Cross sections calculated in *standard kinematics*. The standard results (full lines) are compared with those obtained with the optical potential of Comfort and Karp [37] (dotted lines) and that of Nadasen *et al.* [36] (dashed lines).

respect to the SRC effects.

In this section we discuss the sensitivity of our results to the presence of the Δ currents. There are various aspects of the description of electromagnetically induced Δ excitation that are still largely debated [38, 39]. It is not our aim to enter in this discussion. We have considered a Δ current model commonly used in the literature, we have applied it to two-nucleon emission processes, and we have analyzed the sensitivity of our results to the changes of the parameters of the model and of the kinematics.

We present in Fig. 9 some specific result obtained in *standard kinematics* for $\omega = 100$ MeV and $\omega = 200$ MeV with the aim of discussing two different features regarding the Δ currents. The first one is related to the sensitivity of the results to the various coupling constants defined in Eq. (16). The second one concerns the relative importance of SRC and Δ currents with respect to the change of the excitation energy.

Out of the three constants $f_{\pi NN}$, $f_{\pi N\Delta}$ and $f_{\gamma N\Delta}$, only the first one is rather well defined by the experimental data. Its commonly accepted value is $f_{\pi NN}^2/4\pi=0.079$. The values of the other two constants are not so precisely known. In our *standard calculations* we used the values taken from [40]. In Figs. 9 we have also used the values adopted in Refs. [12] and [17] (see Table 3).

We have also tested the validity of the static approximation in the description of the Δ propagator. This approximation consists essentially in setting $G_A = G_B = 1/(m_\Delta - m_n)$ in Eq. (19). This is the approximation we have used in our previous works [1, 3, 4]. The dotted lines of Fig. 9 show the

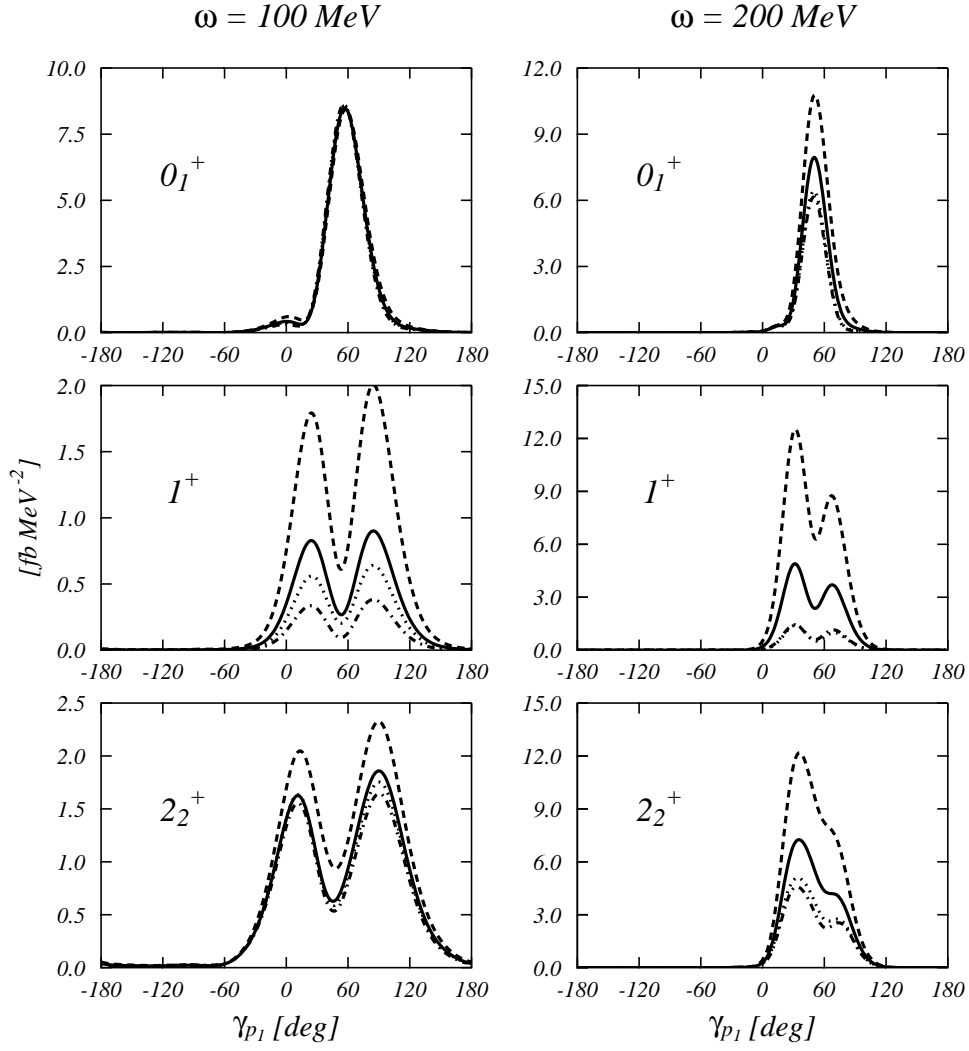


Figure 9: Cross sections for the $^{16}\text{O}(e,e'2p)^{14}\text{C}$ process calculated using different values of the Δ current coupling constants (see Table 3). The full lines have been obtained with the parameters of Ref. [9], and these are the values used in our *standard* calculations. The dashed and dashed dotted lines have been obtained with the parameters of Refs. [12] and [17] respectively. Dotted curves correspond to the *standard* calculations but using the static propagator for the Δ currents.

	AMA	GIU	RYC
$f_{\gamma N\Delta}$	0.299	0.373	0.120
$f_{\pi N\Delta}$	1.69	2.15	2.15

Table 3: Values of the parameters used in Eq. (16). The AMA, GIU and RYC values are from Refs. [40], [12] and [17] respectively.

results obtained with the static approximation.

We observe that at $\omega = 100$ MeV the 0_1^+ state shows scarce sensitivity to the changes of the values of the Δ currents coupling constants. More sensitive is the 2_2^+ state, but certainly the most sensitive one is the 1^+ . These different degrees of sensitivity are connected to the relative importance of the Δ current contribution with respect to the SRC in the various excited states. As already pointed out in Refs. [12] and [17], the 1^+ state is strongly dominated by the Δ currents, therefore any change in the coupling constants produces large modifications of the cross section. The small sensitivity of the 0_1^+ state is due to the fact that its excitation is mainly due to the longitudinal response (see Fig. 11), while the Δ acts on the transverse response only. The Δ contribution is not negligible for the 2_1^+ state and it becomes dominant for the 1^+ .

The results of the static approximation have been obtained by using the constants of Ref. [40]. This approximation is valid when its results are closed to those shown by the full lines. At $\omega=100$ MeV this is the case for all the states we have investigated but the 1^+ . We do not show the results for the 0_2^+ and 2_1^+ states that present analogous features of 0_1^+ and 2_2^+ results.

The situation changes for the excitation energy $\omega=200$ MeV. Now we are in the resonant region of the Δ and here all the states are strongly sensitive to the different values of the coupling constants. The transverse response dominates also in the 0_1^+ state. The results of the static approximations are quite far from the full lines, clearly showing the inadequacy of this approximation. It is interesting to notice that the static approximation produces results rather similar to those obtained with the coupling constants of Ref. [17].

We have investigated the energy and the momentum dependence induced by the SRC and by the Δ currents. The results of our study about the energy dependence are summarized in Fig. 10, where in the left panels we show the cross sections calculated using only the one-body currents plus SRC, while in the right panels we show the results obtained with the Δ currents alone. The comparison between the left and right panels for the 1^+ state, clearly show that the calculations with the Δ currents produce cross sections much larger than those obtained with one-body currents only. This confirms that the excitation of this state is dominated by the Δ currents dynamics. The same analysis requires a more careful discussion in the case of the 0_1^+ state. At $\omega = 100$ and 150 MeV, the cross sections obtained with the one-body currents are larger than those calculated with the Δ currents alone by a factor 20-30. At $\omega = 200$ MeV the difference between the two results is about five times smaller. This indicates that, even for the 0_1^+ state, the contribution of the Δ currents becomes important when the excitation energy is in the Δ resonance region. For the 2_2^+ state the contributions of the one-body and of the Δ currents have the same order of magnitude.

The SRC do not show specific energy dependence. We have verified that by calculating all the ^{16}O final states of Table 1. In the example shown in Fig. 10 one can observe that in the 0_1^+ state the cross sections at 200 MeV is smaller than at 150 MeV, while the size of the cross sections for these excitation energies is almost the same for the 2_2^+ state. The situation is different for the case of the Δ currents whose contribution grows with the energy since it enters in its resonance region.

Some results of our investigation of the momentum transfer dependence are shown in Fig. 11. In this figure, instead of the cross sections, we present the longitudinal and transverse responses, Eqs. (10) and (11), to get rid of the trivial \mathbf{q} dependent terms in the kinematics factors. We show the responses for the 0_1^+ and 1^+ final states.

The 0_1^+ state is dominated by the longitudinal response. The shape of the angular distribution of w_l is not modified by the change of $|\mathbf{q}|$, however its peak value is reduced with increasing $|\mathbf{q}|$. The values of w_t without Δ currents are so small to be negligible. The inclusion of the two-body currents enhances the transverse response. It has been shown in Ref. [14] that, in this state, the emission of the two nucleons is dominated by a relative s -wave. The $|\mathbf{q}|$ dependences of longitudinal and transverse responses are quite different. At $|\mathbf{q}| = 300$ and 400 MeV/c, the longitudinal responses are much larger than the transverse ones. The peak values of the responses become smaller with increasing $|\mathbf{q}|$, but the decrease of w_l is steeper than that of w_t . At $|\mathbf{q}|= 600$ MeV/c we are in a situation where the size of the two responses is about the same. In this kinematics the presence of the Δ currents noticeably affect the full cross section.

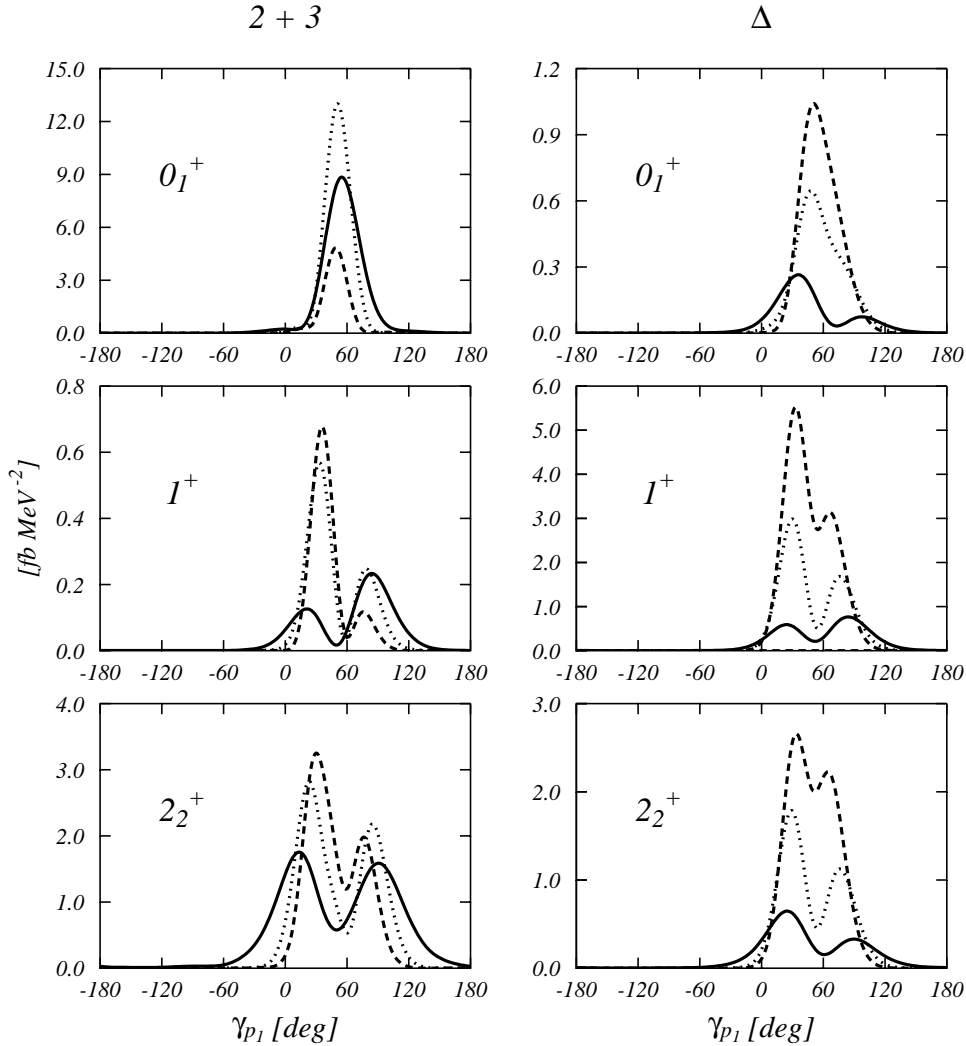


Figure 10: Cross sections for the $^{16}\text{O}(e,e'2p)^{14}\text{C}$ process calculated for three values of the excitation energy. Full lines $\omega=100$ MeV, dotted lines $\omega=150$ MeV, dashed lined $\omega=200$ MeV. The left panels show the results obtained by considering only the one-body currents plus the SRC. The right panels show the cross sections obtained with Δ currents only.

The situation is different for the 1^+ state. This state is dominated by the Δ currents, therefore the transverse response is the most important one. The emission of the two protons is ruled by a relative p -wave [14], which produces an angular distribution with two peaks. These two peaks are clearly visible when the kinematics verifies $\mathbf{q} \approx \mathbf{p}_1 + \mathbf{p}_2$. If $\mathbf{q} \gg \mathbf{p}_1 + \mathbf{p}_2$ for any value of γ_{p_1} , the two peaks merge as it is shown by the dashed and dashed dotted lines. The change of $|\mathbf{q}|$ does not modify sensitively the size of the peaks.

To summarize the results of this section, we may say that, in order to minimize the effects of the Δ currents, one has to work at excitation energies far from the resonance peak, at relatively low values of the momentum transfer ($|\mathbf{q}| \leq 500$ MeV/c), and furthermore one should not consider the 1^+ state.

4.4 The Short Range Correlation

After having studied the sensitivity of our results to the theoretical inputs and to the presence of the Δ currents, we arrive now to the main point of our investigation: the sensitivity of the cross section to the details of the correlation function. It is obvious that the use of very different correlations would produce rather different results, since $f(r)$ is the key ingredient of the calculation. The point is to investigate the sensitivity of the cross section to relatively small changes of realistic correlation functions.

For our investigation we have considered the purely scalar correlation functions $f(r)$ shown in Fig.

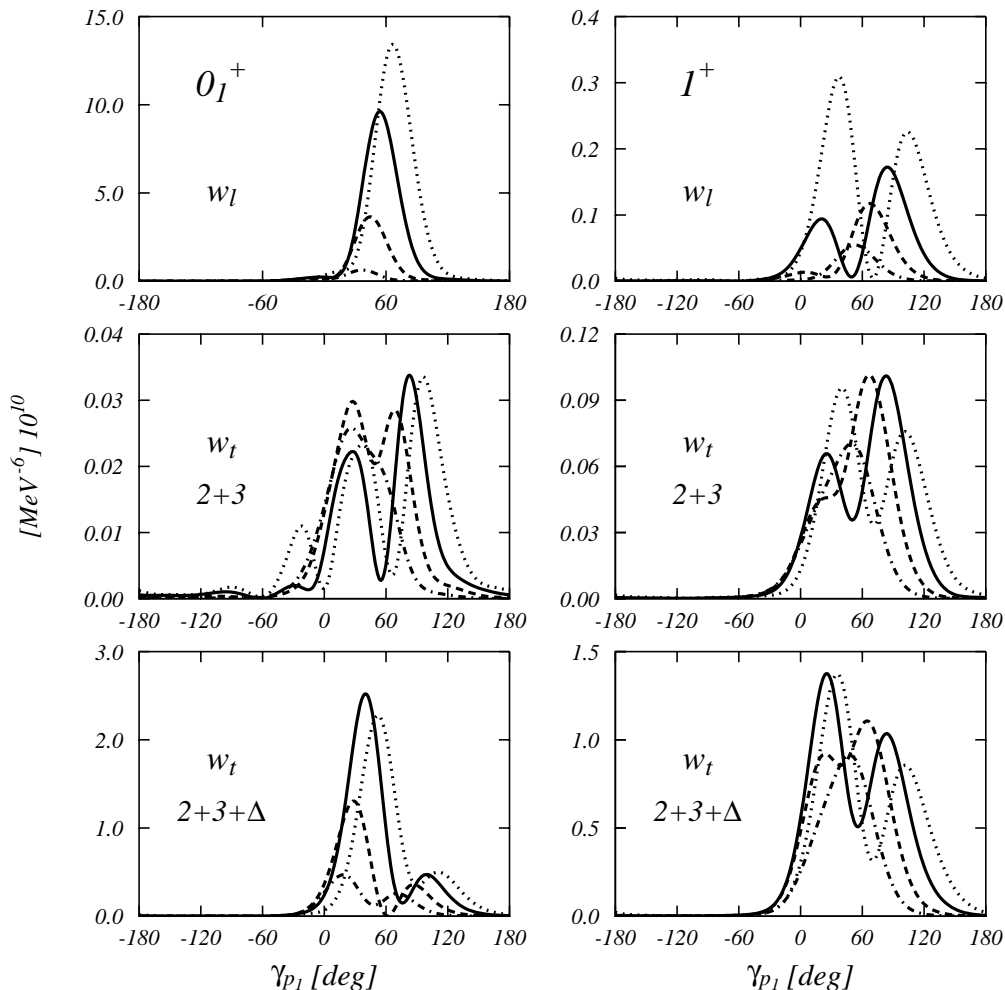
$^{16}\text{O} (e, e' 2p) ^{14}\text{C}$


Figure 11: Longitudinal (w_l) and transverse (w_t) responses, Eqs. (10) and (11), calculated in standard kinematics, for various values of the momentum transfer: dotted lines 300 MeV/c, full lines 400 MeV/c, dashed lines 500 MeV/c and dashed-dotted lines 600 MeV/c. The two central panels have been calculated without Δ currents contribution, while the curves of the lower panels include also this contribution.

12. The correlation function G , we have used up to now, and the $S3$ correlation function, are taken from Ref. [32]. They have been fixed by minimizing the energy functional calculated with a nuclear hamiltonian containing the Afnan and Tang nucleon-nucleon interaction [33]. The two minimizations have been done by considering respectively a gaussian type correlation (G) and the Euler procedure described in that reference ($S3$). The correlation labeled as $V8$ in the figure, is the scalar part of the state dependent correlation used in Ref. [35], where the hamiltonian was built by using the nucleon-nucleon Argonne $V8'$ interaction plus the Urbana IX three-body force. The three correlation functions differ for few details. The $S3$ and $V8$ overshoot the asymptotic value of 1 in the region between 1 and 2 fm. The $V8$ correlation function has a lower minimum than the other two.

In the Figs. 13, 14 and 15 we show the cross sections calculated in *standard kinematics* with the three correlation functions shown in Fig. 12 for three target nuclei: ^{12}C , ^{16}O and ^{40}Ca . The list of the two-hole wave functions describing the final states of the $A - 2$ rest nuclei is given in Table 1.

Apart from details related to the specific nucleus and the final state considered, the general trend shown by these results is that the shapes of the angular distributions are not modified by the correlations. It is rather the size of the cross sections in their maxima which has changed. This indicates that the shapes of the angular distributions are ruled by the kinematics and by the angular momentum coupling between the hole states and the allowed partial waves where the two particles can be emitted. This has been widely discussed in [14] where a decomposition of the partial wave in terms of center

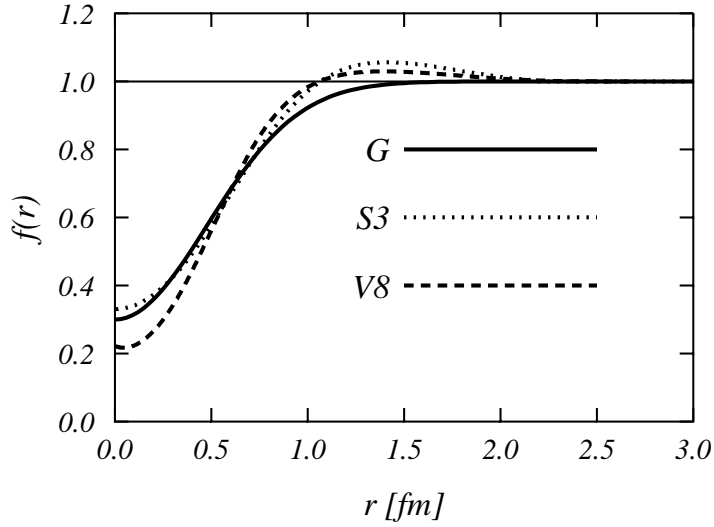


Figure 12: Correlation functions used in our calculations. The line labeled G indicates the gaussian correlation function of Ref. [32] and that labeled $S3$ the Euler correlation function of the same reference. With $V8$ we show the scalar term of the state dependent correlation function of Ref. [35].

of mass and relative motion of the emitted nucleon pair has been done.

The cross sections obtained by using the $V8$ and $S3$ correlations are rather similar and they are roughly a factor two smaller than those obtained with the gaussian correlation, which we took as *standard* results. This effect is certainly larger than the theoretical uncertainties estimated in section 4.2. The 1^+ states are out of systematics because they are dominated by the Δ currents.

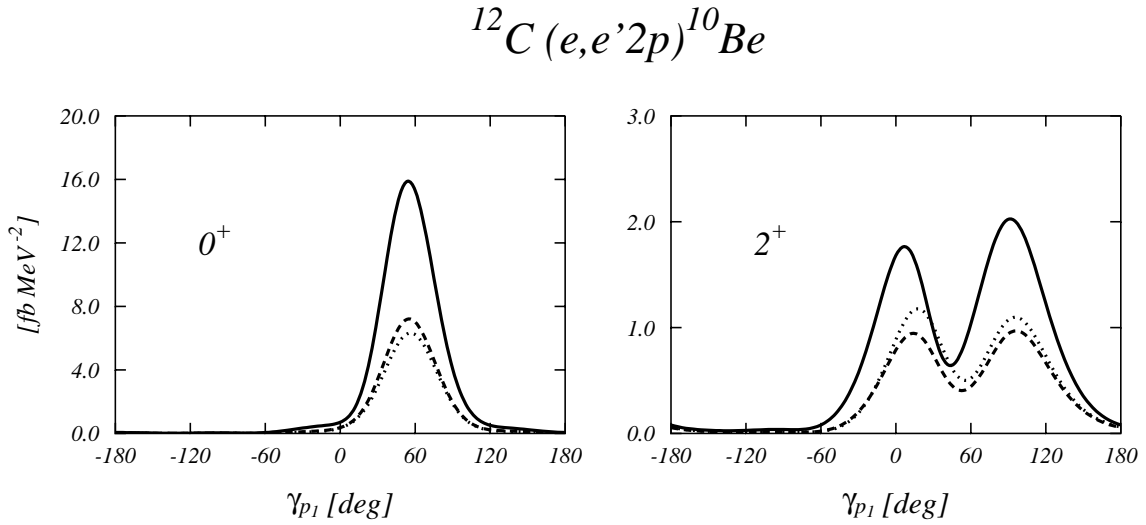


Figure 13: $^{12}\text{C}(e,e'2p)^{10}\text{B}$ cross section in the *standard kinematics* for the emission of the two proton from the $1p_{3/2}$ level of the target nucleus. The full, dotted and dashed lines, have been obtained by using respectively the G , $S3$ and $V8$ correlation functions of Fig. 12.

To investigate the sources of these differences we have done calculations with rather schematic correlations which allowed us to switch on and off various characteristics of the correlation functions.

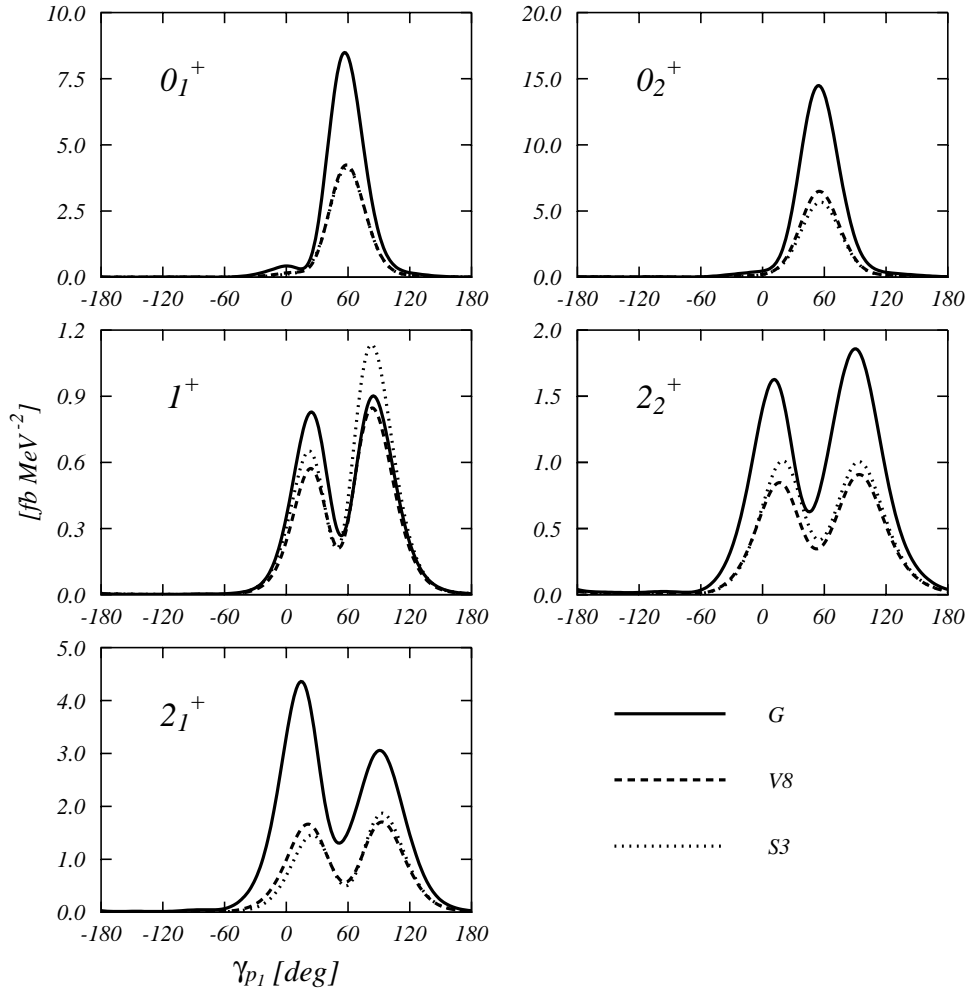
$^{16}\text{O}(e,e'2p)^{14}\text{C}$


Figure 14: $^{16}\text{O}(e,e'2p)^{14}\text{C}$ cross sections calculated in *standard kinematics* with the three correlation functions shown in Fig. 12.

To this purpose we used step function correlations of the type

$$f(r) = \begin{cases} A, & 0 \leq r < d_1 \\ B, & d_1 \leq r < d_2 \\ 1.0, & d_2 \leq r \end{cases} \quad (41)$$

We have changed the values of the A, B, d_1 and d_2 parameters to produce four different correlations. The values of the parameters used in our calculations are given in Table 4.

	A	B	d_1 [fm]	d_2 [fm]
CSC1	0.2	1.0	1.0	1.0
CSC2	0.1	1.0	1.0	1.0
CSC3	0.2	1.1	1.0	1.3
CSC4	0.2	1.0	0.9	0.9

Table 4: Parameters of the schematic correlation functions as given into Eq. 41.

The correlation function *CSC1* is a square well of radius 1.0 fm and depth 0.2. The $^{16}\text{O}(e,e'2p)^{14}\text{C}$ cross sections calculated in *standard kinematics* with this correlation function are shown in Fig. 16 by

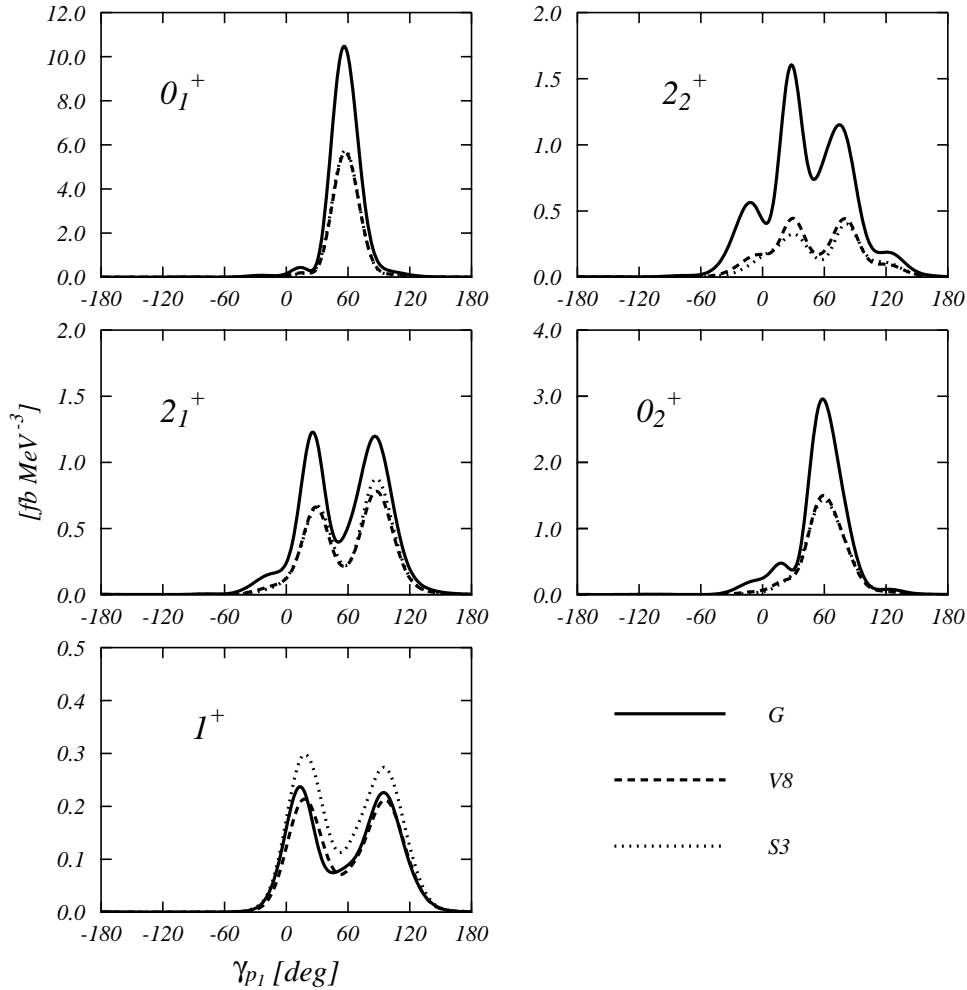
$${}^{40}\text{Ca}(e,e'2p){}^{38}\text{Ar}$$


Figure 15: ${}^{40}\text{Ca}(e,e'2p){}^{38}\text{Ar}$ cross section calculated in the *standard kinematics*. The full, dotted and dashed lines, have been obtained by using respectively the G , $S3$ and $V8$ correlation functions of Fig. 12.

the full lines. We shall discuss the differences produced by changing the correlations with respect to these results. The correlation function $CSC2$ has the same shape of $CSC1$ but a lower minimum. The effect is a small increase of the cross sections (see dashed curves). The $CSC3$ correlation function has a square shape of the type of that of $CSC1$ but, for $1.0 \text{ fm} \leq r \leq 1.3 \text{ fm}$, it overshoots the asymptotic value of 1.0. This modification in the correlation function is enough to lower to half, roughly, the cross section maxima (dotted curves). An analogous effect is obtained by the $CSC4$ which has the same shape as $CSC1$ but a smaller healing radius. The results obtained with this last correlation function are shown by the dashed-dotted curves.

The behaviors just described can be understood by remembering that the quantity entering in the cross section calculation is not $f(r)$ but rather $h(r) = f^2(r) - 1$. The largest is the contribution of $h(r)$ in Eq. (37), the largest are the cross sections. The $CSC2$ correlation has a larger overlap with the other integrated functions than $CSC1$, since its depth is deeper. The overshooting in $CSC3$ generates a term in $h(r)$ of opposite sign with respect to the rest of the function, therefore the total contribution to the integral becomes smaller. The same effect can be obtained by reducing the range of the correlation, as it is done in $CSC4$.

It is now easier to understand the results of Figs. 13, 14 and 15. The three correlations used in the calculations reach their asymptotic values at about the same internucleon distance: 2 fm. The $S3$ and $V8$ correlation functions overshoot this value in the region between 1 fm and 2 fm. This part has opposite effects as the part below the value of 1, as it has been showing the case of $CSC3$. Since these functions should be multiplied by a r^2 in the integral, the effect of the overshooting is larger than the

$^{16}\text{O} (e, e' 2p) ^{14}\text{C}$

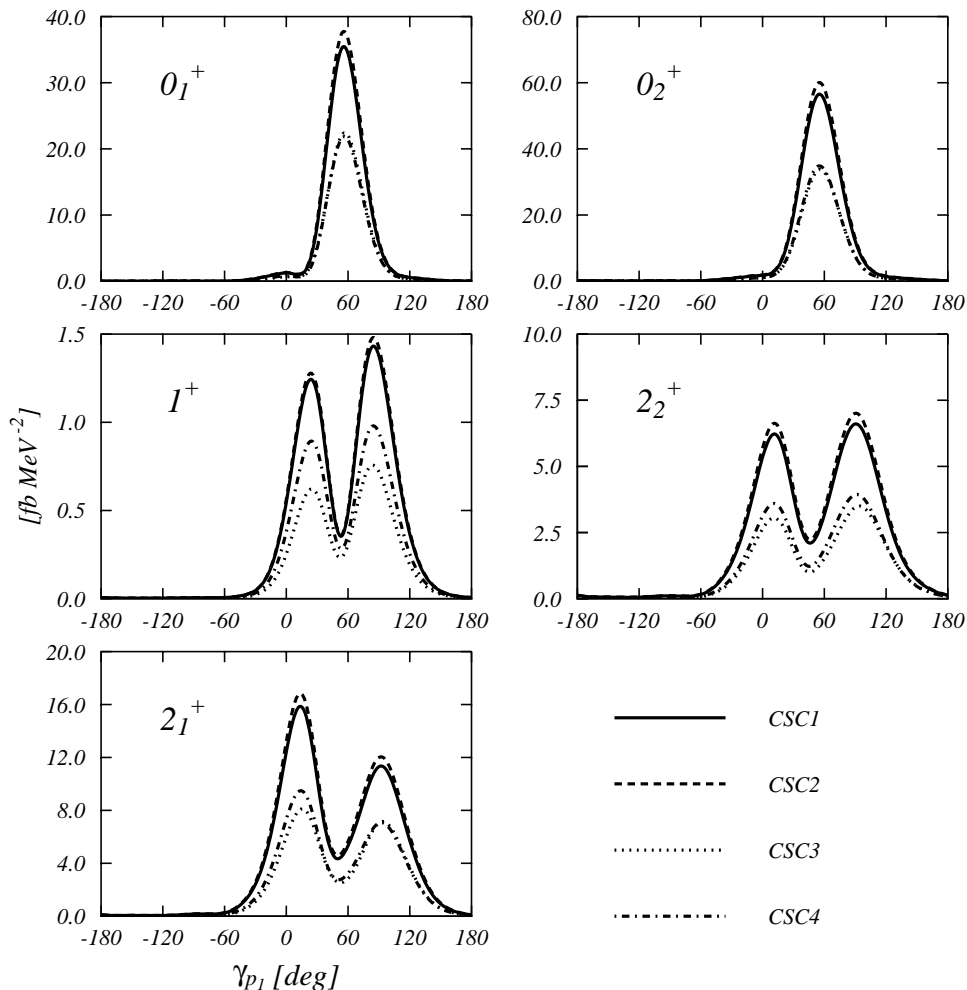


Figure 16: Cross section in *standard kinematics* calculated with the schematic correlations of Eq. (41) using the parameters given Table 4.

small differences in the minima at $r = 0$ fm.

It is remarkable that very schematic correlation functions as those used in Fig. 16 produce angular distributions with the same form as those of Fig. 14, obtained with realistic correlation functions. This confirms again that the shapes of the angular distributions are determined by the quantum numbers of the final states.

We have tested the role of various diagrams considered in our model. In Fig. 17 the cross sections calculated in the *standard kinematics* and with the gaussian correlation function are presented. The dotted lines have been obtained by using the 2-point diagrams of Fig. 3. The dashed lines show the results we got when 2 and 3-point diagrams of Fig. 3 are used. The total results when also the Δ current contributions are added are presented by the full lines.

The inclusion of the 3-point diagrams lowers the cross sections calculated with the 2-point diagrams only in all the cases we have considered. This reduction is not constant but it depends from γ_{p_1} , as it is clearly shown by the two 2^+ states where the peaks around $\gamma_{p_1}=0$ are more quenched than those around $\gamma_{p_1}=100^\circ$. The effect of the Δ currents does not have a regular behavior. The global quenching of the cross section shown in 0_1^+ is followed by an enhancement in the 0_2^+ state not shown in the figure. Also the two 2^+ states show different behavior of the Δ currents. As already mentioned the 1^+ is dominated by the Δ currents even at 100 MeV.

We have already mentioned that $\mathbf{p}_r = \mathbf{q} - \mathbf{p}_1 - \mathbf{p}_2$ is a crucial quantity in the two nucleon emission process. We have changed this quantity in our *standard kinematics* by modifying the γ_{p_2} angle. In Fig. 18 we present some of the results we have obtained using $\gamma_{p_2}=30^\circ$ (dotted lines), $\gamma_{p_2}=60^\circ$ (full

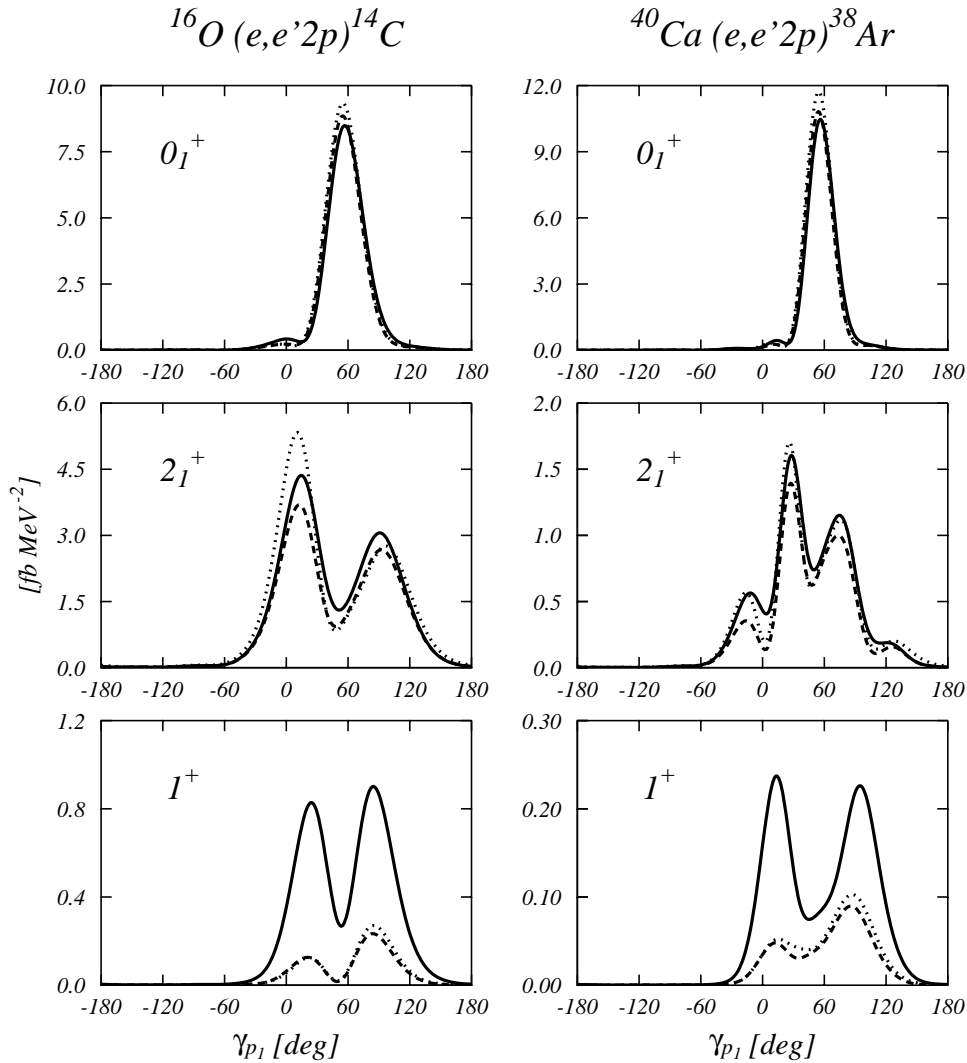


Figure 17: Two nucleon emission cross sections calculated in *standard kinematics*. The dotted lines have been obtained considering only the 2-point diagrams of Fig. 3. The dashed lines have been obtained by adding the 3-point diagrams and the full lines show the results when also the Δ currents are included. The gaussian correlation of Fig. 12 has been used.

lines) and $\gamma_{p_2}=90^\circ$ (dashed lines).

It is interesting to notice that the angular distributions of the 0^+ states do not change their form by changing γ_{p_2} , only the size of the peak is modified. The situation is rather different for the 2^+ states. By changing γ_{p_2} there is a merging of the two peaks which are well separated at $\gamma_{p_2}=60^\circ$. This situation is analogous to that discussed in the description of Fig. 11.

5 SUMMARY AND CONCLUSIONS

We have studied electron induced two-nucleon emission processes by applying a model which has been already used to describe inclusive [1, 10] and one nucleon emission processes [2, 3]. In this model, inspired to the correlated basis function theory, the full cluster expansion is truncated to consider all, and only, those diagrams containing a single correlation function $h(r)$.

In addition to the traditional two-point diagrams, evaluated also in other approaches [12, 17], we consider also three-point diagrams. These diagrams are necessary to conserve the proper normalization of the nuclear final state. The presence of these tree-point diagrams always reduces the two-point cross sections. From the quantitative point of view, in the kinematics we have investigated, we found relevant effects only for the 2^+ final states, where we could detect differences of about 40%. In all the other cases the role of the three-point diagrams is much smaller.

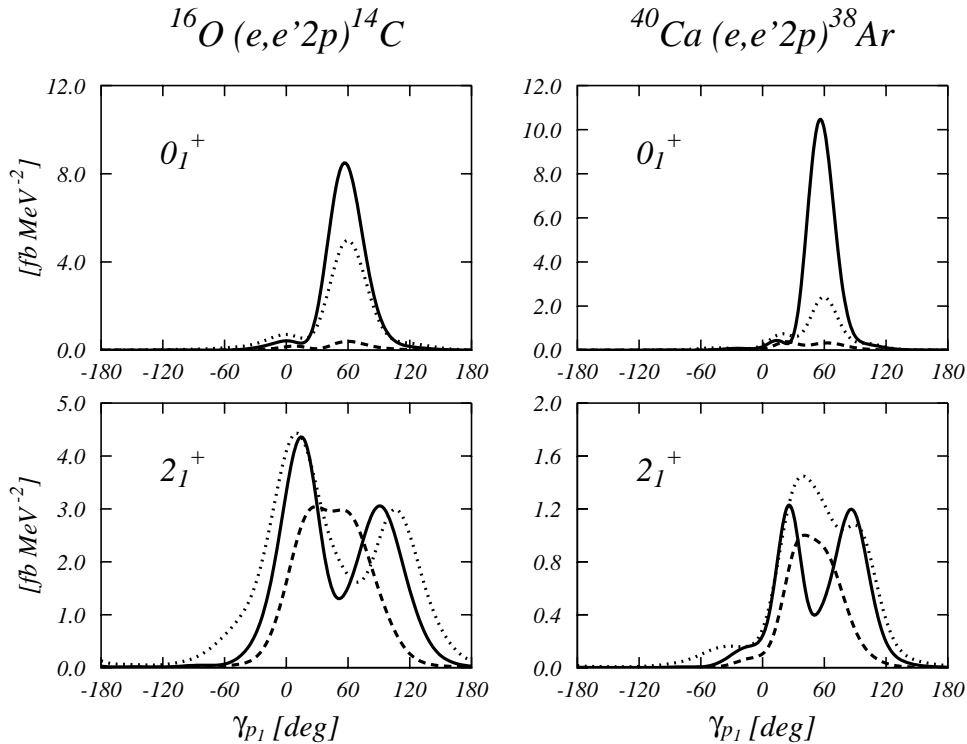


Figure 18: Cross sections calculated in the *standard kinematics* but changing the value of the γ_{p_2} angle. Dotted lines $\gamma_{p_2}=30^\circ$, full lines $\gamma_{p_2}=60^\circ$ and dashed lines $\gamma_{p_2}=90^\circ$.

We have shown two-proton emission cross sections as a function of the angle of one of the emitted protons. Because of the energy and momentum conservation, Eqs. (38) and (39), this kinematic set up implies the change of the energy of the proton for every emission angle. We have used an approximation consisting in neglecting the recoil of the $A - 2$ residual nucleus, therefore the energy of the emitted nucleons is the same for every emission angle. This approximation works well in the region where the cross sections have their maxima. This indicates that these maxima appears when the recoil momentum of the residual nucleus has its minimum value, as was already discussed in [12, 16, 17]. Since the cross sections values drop by several order of magnitude in the regions outside the maximum, we used this no-recoil approximation in our study.

We have investigated the sensitivity of our results to the possible changes of the mean-field input. We have modified the mean field parameters such as the description of the nuclear data different from (e,e'2p) reaction would not be compromised. For example, the hole wave functions have been modified but we always cared to reproduce the charge root mean square radii. We used different optical potentials taken from the literature but all of them reproduce elastic scattering proton-nucleus data in different energy regimes. We have estimated that plausible changes of the mean-field bases would imply a theoretical uncertainty of about 20% - 30% on the maxima of the (e,e'2p) cross section.

The cross sections are most sensitive to the changes in the particle wave functions. Calculations done considering these wave functions to be plane waves, or by using purely real Woods-Saxon waves, show cross sections a factor two larger than those obtained with a complex optical potential. A consistent description of the one nucleon emission processes [2, 3] requires the use of complex optical potentials to take into account the excitation of emission channels different from the one considered. The effects of changing optical potential are certainly smaller than those produced by the use of real mean-field, but they are not irrelevant. In the kinematics we have studied we found changes as large as 18%.

The presence of the two-body Δ currents interferes with the SRC in the two-nucleon emission mechanism. To minimize the effects of the Δ currents one has to find proper kinematics conditions. We found that the role of these two-body currents at excitation energy $\omega=200$ MeV is always relevant for every final state. This is reasonable since 200 MeV is well inside the Δ resonance region.

The situation changes for $\omega=100$ MeV. The 0^+ states leaving the residual nuclei in their ground states are rather insensitive to the Δ currents for $|\mathbf{q}| \leq 500$ MeV/c, since their excitation is mainly of longitudinal type. The 1^+ states are instead excited via transverse responses and, even at 100 MeV, they are strongly affected by the presence of the Δ . The situation is intermediate for the 2^+ states where both longitudinal and transverse excitations are important.

The test of sensitivity of the cross section on the details of the correlation function has been done by using three different correlation functions taken from Fermi hypernetted chain calculations on finite nuclear systems [32, 35]. These are realistic correlation functions and differ only for few details.

A first remark about our results is that the shape of the angular distributions of the cross sections remain essentially unchanged. This shape is insensitive to the correlations and it is determined by the decaying waves allowed by the angular momentum and parity composition related to the quantum number of the nuclear final state. We essentially confirm the arguments of Ref. [14] where a partial wave decomposition of the various nuclear final states is presented.

We have already mentioned that the maxima appear to emission angles corresponding to the minimum values of the nuclear recoil momentum \mathbf{p}_r . The modification of the shapes due to the changes of the kinematics can be understood in terms of Fourier transform of the two-hole relative wave function with respect to \mathbf{p}_r .

The SRC act on the size of the cross section. Calculations done with a set of schematic correlation functions, allowed us to understand the observed behavior in the results obtained with the realistic correlation functions. The size of the cross section is related to the function $h(r) = f^2(r) - 1$ where $f(r)$ is the two-body correlation function as it is usually defined. The cross section is more sensitive to the length of the healing distance, the distance where $h(r)$ becomes zero, than to the value of $h(r)$ for $r = 0$. An overshooting of the asymptotic value of $f(r)$, corresponding to a change of sign of $h(r)$, produces results similar to those obtained by reducing the length of the healing distance.

The information about the SRC can be obtained only by a quantitative comparison between theoretical predictions and experimental data. Qualitative features, such as the shape of the angular distributions, are not sensitive to the details of the SRC. Unfortunately a precise quantitative evaluation of the (e,e'2p) cross sections is linked to the theoretical framework used to calculate it, and to the uncertainties in the required theoretical input. It appears clear that two-nucleon knock out experiments cannot be considered as the ultimate tool able to determine the characteristics of the SRC correlations. Instead, they have to be considered as another, useful and interesting, element of a puzzle, that together with elastic, inclusive and one-nucleon emission experiments should be described in a unique and coherent theoretical framework.

APPENDIX A: Matrix elements of the one-body operators

In this appendix we give the explicit expressions of the matrix elements (31) needed to evaluate the response functions of Eqs. (10)-(13). Actually, what we calculate is the ξ^1 term as defined in Eq. (37). The calculation of the various terms defining this transition matrix element proceeds by making a multipole expansion of the correlation function h_{ij} :

$$h_{ij} = h(r_{ij}) = h(r_i, r_j, \cos \theta_{ij}) = \sum_{L=0}^{\infty} h_L(r_i, r_j) P_L(\cos \theta_{ij}), \quad (42)$$

where P_L are the associated Legendre polynomials.

As shown in Eq. (32), the operator $O_\eta(\mathbf{q})$ is the Fourier transform of a one-body operator, in our case the electromagnetic operators (14) and (15). We perform a multipole expansion of the $e^{-i\mathbf{q}\cdot\mathbf{r}}$ term and, because we have chosen the z -axis parallel to the direction of the momentum transfer \mathbf{q} we obtain

$$O_0(\mathbf{q}) \equiv \rho(\mathbf{q}) = \sqrt{4\pi} \sum_J (-i)^J \hat{J} \int d^3r j_J(qr) Y_{J0}(\Omega) \rho(\mathbf{r}), \quad (43)$$

$$O_{\pm 1}(\mathbf{q}) \equiv J_{\pm 1}(\mathbf{q}) = \sqrt{2\pi} \sum_J (-i)^J \hat{J} \int d^3r \left[(-i)^{-1} \frac{\sqrt{J+1}}{\hat{J}} j_{J-1}(qr) \mathbf{Y}_{J-1,1,J}^{\pm 1}(\Omega) \right. \\ \left. \pm j_J(qr) \mathbf{Y}_{J,1,0}^{\pm 1}(\Omega) + (-i) \frac{\sqrt{J}}{\hat{J}} j_{J+1}(qr) \mathbf{Y}_{J+1,1,J}^{\pm 1}(\Omega) \right] \cdot J(\mathbf{r}), \quad (44)$$

where we have indicated with

$$\mathbf{Y}_{\lambda,1,J}^M(\Omega) = \sum_{\mu\eta} \langle \lambda\mu 1\eta | JM \rangle Y_{\lambda\mu}(\Omega) e_{\eta} \quad (45)$$

the vector spherical harmonics [29] and with j_{λ} the spherical Bessel functions. In the above equations we have defined $\hat{l} = \sqrt{2l+1}$.

From the above equations and the expressions (14) and (15) we found convenient to express each multipole component of the one-body operator operator O_{η} in terms of products of a factor depending on qr and another one depending only on the angular coordinates Ω . For the charge operator ($\eta = 0$) we have

$$O_0(\mathbf{q}) = \sum_J \int d^3r F_J(qr) \mathcal{O}_{J,0}(\Omega). \quad (46)$$

By taking into account Eqs. (14) and (43) we identify

$$F_J(qr) = \sqrt{4\pi} (-i)^J \hat{J} j_J(qr) \sum_{i=1}^A \left[G_E^P(\mathbf{q}) \frac{1 + \tau_3(i)}{2} + G_E^N(\mathbf{q}) \frac{1 - \tau_3(i)}{2} \right], \quad (47)$$

and

$$\mathcal{O}_{J,0}(\Omega) = Y_{J0}(\Omega). \quad (48)$$

In the above equation we have indicated with $G_E^{P,N}(\mathbf{q})$ the electric form factor of the proton and neutron, respectively.

For the magnetization current ($\eta = \pm 1$) we have

$$O_{\pm 1}(\mathbf{q}) = \sum_J \int d^3r \sum_{s=\pm 1,0} F_J^s(qr) \mathcal{O}_{J,\pm 1}^s(\Omega). \quad (49)$$

Taking into account Eqs. (15) and (44) the factors in the previous equation are defined as:

$$F_J^s(qr) = \sqrt{2\pi} (-i)^J \Gamma(J, s) j_{J+s}(qr) \sum_{i=1}^A \left[\frac{G_M^P(\mathbf{q})}{2m_i} \frac{1 + \tau_3(i)}{2} + \frac{G_M^N(\mathbf{q})}{2m_i} \frac{1 - \tau_3(i)}{2} \right], \quad (50)$$

with $G_M^{P,N}(\mathbf{q})$ the nucleon magnetic form factor and

$$\Gamma(J, s) = \begin{cases} -i\eta \sqrt{J + \delta_{s,-1}}, & s = -1 \\ \hat{J}, & s = 0 \\ i\eta \sqrt{J}, & s = +1 \end{cases}, \quad (51)$$

and

$$\mathcal{O}_{J,\eta}^s(\Omega) = [Y_{J+s}(\Omega) \otimes \boldsymbol{\sigma}]_{\eta}^J. \quad (52)$$

In the following, the coordinate where the one-body operators is acting will be labeled r_1 . The same notation has been used in Eq. (37). For the charge we define the integrals

$$K(q; J; a, b) \equiv \int dr_1 r_1^2 F_J(qr_1) R_a^*(r_1) R_b(r_1), \quad (53)$$

$$I(q; J, L; a, b, c, d) \equiv \int dr_1 r_1^2 \int dr_2 r_2^2 h_L(r_1, r_2) F_J(qr_1) R_a^*(r_1) R_b^*(r_2) R_c(r_1) R_d(r_2), \quad (54)$$

and

$$H(L; a, b, c, d) \equiv \int dr_1 r_1^2 \int dr_2 r_2^2 h_L(r_1, r_2) R_a^*(r_1) R_b^*(r_2) R_c(r_1) R_d(r_2), \quad (55)$$

where R is the radial part of the single particle wave function defined in Eq. (24). Similar expressions are defined for the current operator by changing $F_J(qr_1)$ into $F_J^s(qr_1)$ in the K and I integrals.

The orthonormality of the single particle basis used to construct the Slater determinants $|\Phi_f\rangle$ and $|\Phi(0,0)\rangle$ ensures that only the single particle wave functions directly involved by the electromagnetic operator and by the correlation function contribute to the matrix elements.

Following the nomenclature of the diagrams shown in Fig. 3 we obtain

$$\begin{aligned} \langle O \rangle_{(2.1)} \equiv & \sum_{JL\lambda} I(q; J, L; p_1, p_2, h_1, h_2) \delta_{t_{p_1}, t_{h_1}} \delta_{t_{p_2}, t_{h_2}} \frac{4\pi}{\widehat{L}^2} \widehat{\lambda} (-1)^{J-L+\eta+j_{p_1}-m_{p_1}+j_{p_2}-m_{p_2}} \\ & \begin{pmatrix} J & L & \lambda \\ \eta & -N & N-\eta \end{pmatrix} \begin{pmatrix} j_{p_1} & \lambda & j_{h_1} \\ -m_{p_1} & -N+\eta & m_{h_1} \end{pmatrix} \begin{pmatrix} j_{p_2} & L & j_{h_2} \\ -m_{p_2} & N & m_{h_2} \end{pmatrix} \\ & \langle j_{p_1} || [\mathcal{O}_J \otimes Y_L]^\lambda || j_{h_1} \rangle \langle j_{p_2} || Y_L || j_{h_2} \rangle, \end{aligned} \quad (56)$$

where $\delta_{a,b}$ is the Kronecker symbol. The expression of the (2.2) diagram is obtained from the above one by interchanging h_1 and h_2 . The expressions of the (2.3) and (2.4) diagrams are obtained by interchanging p_1 with p_2 in the expressions of the (2.1) and (2.2) diagrams, respectively.

For the three-point diagrams we have

$$\begin{aligned} \langle O \rangle_{3.1} \equiv & \sum_{JL} \sum_i K(q; J; p_1, i) H(L; i, p_2, h_1, h_2) \delta_{t_{p_1}, t_i} \delta_{t_i, t_{h_1}} \delta_{t_{p_2}, t_{h_2}} \\ & \frac{4\pi}{\widehat{L}^2} (-1)^{j_{p_1}-m_{p_1}} (-1)^{j_{p_2}-m_{p_2}} (-1)^{N+j_i-m_i} \\ & \begin{pmatrix} j_{p_1} & J & j_i \\ -m_{p_1} & \eta & m_i \end{pmatrix} \begin{pmatrix} j_{p_2} & L & j_{h_2} \\ -m_{p_2} & N & m_{h_2} \end{pmatrix} \begin{pmatrix} j_i & L & j_{h_1} \\ -m_i & -N & m_{h_1} \end{pmatrix} \\ & \langle j_{p_1} || \mathcal{O}_J || j_i \rangle \langle j_{p_2} || Y_L || j_{h_2} \rangle \langle j_i || Y_L || j_{h_1} \rangle. \end{aligned} \quad (57)$$

The expression of the diagram (3.2) is analogous to the above one but interchanging h_1 with h_2 . The (3.3) and (3.4) diagrams are obtained by interchanging p_1 and p_2 in the (3.1) and (3.2) diagrams respectively. For the other diagrams we have:

$$\begin{aligned} \langle O \rangle_{3.5} \equiv & \sum_{JL} \sum_i K(q; J; i, h_2) H(L; p_2, p_1, i, h_1) \delta_{t_i, t_{h_2}} \delta_{t_{p_2}, t_i} \delta_{t_{p_1}, t_{h_1}} \\ & \frac{4\pi}{\widehat{L}^2} (-1)^{j_i-m_i} (-1)^{j_{p_1}-m_{p_1}} (-1)^{N+j_{p_2}-m_{p_2}} \\ & \begin{pmatrix} j_i & J & j_{h_2} \\ -m_i & \eta & m_{h_2} \end{pmatrix} \begin{pmatrix} j_{p_1} & L & j_{h_1} \\ -m_{p_1} & N & m_{h_1} \end{pmatrix} \begin{pmatrix} j_{p_2} & L & j_i \\ -m_{p_2} & -N & m_i \end{pmatrix} \\ & \langle j_i || \mathcal{O}_J || j_{h_2} \rangle \langle j_{p_1} || Y_L || j_{h_1} \rangle \langle j_{p_2} || Y_L || j_i \rangle. \end{aligned} \quad (58)$$

Also in this case we obtain the expression of the (3.6) diagram from the above expression by interchanging h_1 and h_2 .

The above expressions are specialized for the charge operator. For the magnetization current, \mathcal{O}_J must be changed into $\mathcal{O}_{J,\eta}^s$. The various charge and current transitions are calculated by substituting the above definitions in Eqs. (56)-(58) and remembering that

$$\langle j_a || Y_L || j_b \rangle = (-1)^{j_a+\frac{1}{2}} \frac{\widehat{j}_a \widehat{j}_b \widehat{L}}{\sqrt{4\pi}} \begin{pmatrix} j_a & L & j_b \\ \frac{1}{2} & 0 & -\frac{1}{2} \end{pmatrix} \xi(l_a + l_b + L), \quad (59)$$

$$\langle j_a || [Y_L \otimes Y_J]^K || j_b \rangle = (-1)^{L-J} \frac{\widehat{J} \widehat{L}}{\sqrt{4\pi}} \begin{pmatrix} L & K & J \\ 0 & 0 & 0 \end{pmatrix} \langle j_a || Y_K || j_b \rangle, \quad (60)$$

$$\langle j_a || [Y_J \otimes \sigma]^J || j_b \rangle = (-1)^{l_a} \frac{\widehat{j}_a \widehat{j}_b \widehat{J}}{\sqrt{4\pi}} \begin{pmatrix} j_b & j_a & J \\ -\frac{1}{2} & -\frac{1}{2} & 1 \end{pmatrix} \xi(l_a + l_b + J), \quad (61)$$

$$\begin{aligned} \langle j_a || [Y_{J_s} \otimes \sigma]^J || j_b \rangle &= (-1)^{l_a + l_b + j_b + \frac{1}{2}} \frac{\widehat{j}_a \widehat{j}_b}{\sqrt{4\pi}} \frac{\chi_a + \chi_b + sJ + \delta_{s,1}}{\sqrt{J + \delta_{s,1}}} \\ &\quad \begin{pmatrix} j_a & j_b & J \\ \frac{1}{2} & -\frac{1}{2} & 0 \end{pmatrix} \xi(l_a + l_b + J + 1), \end{aligned} \quad (62)$$

where $|j_a \rangle \equiv |l_b \frac{1}{2} j_a \rangle$, with $\xi(L) = 1$ if L is even and zero otherwise and

$$\chi_a \equiv (-1)^{l_a + j_a + \frac{1}{2}} (j_a + \frac{1}{2}) = (l_a - j_a)(2j_a + 1). \quad (63)$$

ACKNOWLEDGMENTS

We thank Carlotta Giusti for her interest in our work, the numerous discussions and for the careful reading of the manuscript. We also thank Paolo Christillin and Roberto Perrino for useful discussions. This work has been partially supported by the agreement INFN-CICYT, by the DGES (PB98-1367), by the Junta de Andalucia (FQM 225) and by the MIUR through the PRIN *Fisica del nucleo atomico e dei sistemi a molticorpi*.

References

- [1] G. Co' and A. M. Lallena, *Ann. Phys. (N.Y.)* **287** (2001), 101.
- [2] S. R. Mokhtar, M. Anguiano, G. Co' and A. M. Lallena, *Ann. Phys. (N.Y.)* **292** (2001), 67.
- [3] M. Anguiano, G. Co', A. M. Lallena and S.R. Mokhtar, *Ann. Phys. (N.Y.)* **296** (2002), 235.
- [4] M. Anguiano and G. Co', *J. Phys. G*, **27** (2001) 2109.
- [5] A. Fabrocini and G. Co', *Phys. Rev. C* **63** (2001), 044319.
- [6] A. N. Antonov, P. E. Hodgson and I. Zh. Petkov, *Nucleon Momentum and Density Distributions*, Clarendon Press, Oxford, 1988.
- [7] S. Fantoni and V. R. Pandharipande, *Nucl. Phys. A* **473** (1987), 234.
- [8] A. Fabrocini and S. Fantoni, *Nucl. Phys. A* **503** (1989), 375; O. Benhar, A. Fabrocini and S. Fantoni, *Nucl. Phys. A* **550** (1992), 201; A. Fabrocini, *Phys. Rev. C* **55** (1997), 330.
- [9] J.E. Amaro, A.M. Lallena, G. Co' and A. Fabrocini, *Phys. Rev. C* **57** (1998), 3473.
- [10] S.R. Mokhtar, G. Co' and A.M. Lallena, *Phys. Rev. C* **62** (2000), 067304.
- [11] C. Giusti and F.D. Pacati, *Nucl. Phys. A* **535** (1991), 573,
C. Giusti, F.D. Pacati and M. Radici, *Nucl. Phys. A* **546** (1992), 607,
C. Giusti and F.D. Pacati, *Nucl. Phys. A* **571** (1994), 694,
C. Giusti and F.D. Pacati, *Nucl. Phys. A* **585** (1995), 618.
- [12] C. Giusti and F.D. Pacati, *Nucl. Phys. A* **615** (1997), 373.

- [13] W.J.W. Geurts, K. Allaart, W.H. Dickhoff and H. Müther *Phys. Rev. C* **54** (1996), 1144
D. Knödler, H. Müther and P. Czernski *Phys. Rev. C* **61** (2000), 064603
D. Knödler and H. Müther *Phys. Rev. C* **63** (2001), 044602
- [14] C. Giusti, F.D. Pacati, K. Allaart, W.J.W. Geurts, W.H. Dickhoff and H. Müther *Phys. Rev. C* **57** (1998), 1691.
- [15] J. Ryckebusch, M. Vanderhaeghen, K. Heyde and M. Waroquier, *Phys. Lett. B* **350** (1995), 1.
- [16] J. Ryckebusch, *Phys. Lett. B* **383** (1996), 1.
- [17] J. Ryckebusch, V. Van der Sluys, K. Heyde, H. Holvoet, W. Van Nespen, M. Waroquier and M. Vanderhaeghen, *Nucl. Phys. A* **624** (1997), 581.
- [18] L.J.H.M. Kester *et al.*, *Phys. Rev. Lett.* **74** (1995), 1712.
- [19] A. Zondervan *et al.*, *Nucl. Phys. A* **587** (1995), 697.
- [20] C.J.G. Onderwater *et al.*, *Phys. Rev. Lett.* **78** (1997), 4893,
C.J.G. Onderwater *et al.* *Phys. Rev. Lett.* **81** (1998), 2213.
- [21] R. Starink *et al.* *Phys. Lett. B* **474** (2000), 33.
- [22] S. Boffi, C. Giusti, F.D. Pacati and M. Radici, *Electromagnetic Response of Atomic Nuclei* (Clarendon Press, Oxford, 1996).
- [23] J.D. Bjorken and S.D. Drell, *Relativistic Quantum Mechanics*, (McGraw Hill, New York, 1964).
- [24] G. Hoehler, E. Pietarinen, I. Sabba-Stefabescu, F. Borkowski, G.G. Simon, V.H. Walther and R.D. Wendling, *Nucl. Phys. B* **114** (1976), 505.
- [25] Th. Wilbois, P. Wilhelm and H. Arenhövel, *Phys. Rev. C* **54** (1996), 3311.
- [26] P. Wilhelm, H. Arenhövel, C. Giusti and F.D. Pacati, *Z. Phys. A* **359** (1997), 467.
- [27] E. Oset, H. Toki and W. Weise, *Phys. Rep.* **83** (1982) 281.
- [28] J. E. Amaro, G. Co', and A. M. Lallena, *Ann. Phys. (N.Y.)* **221** (1993), 306.
- [29] A.R. Edmonds, *Angular momentum in quantum mechanics*, (Princeton University Press, Princeton, 1957).
- [30] G. Co', *Nuov. Cim. A* **108** (1995), 623.
- [31] S. Boffi, F. Cannata, F. Capuzzi, C. Giusti and F.D. Pacati, *Nucl. Phys. A* **379** (1982), 509
- [32] F. Arias de Saavedra, G. Co', A. Fabrocini and S. Fantoni, *Nucl. Phys. A* **605** (1996), 359.
- [33] I.R. Afnan and Y.C. Tang, *Phys. Rev* **175** (1968), 1337.
- [34] P. Schwandt, H.O. Meyer, W.W. Jacobs, A.D. Bacher, S.E. Vigdor, M.D. Kaitchuck and T.R. Donoghue, *Phys. Rev. C* **26** (1982), 55.
- [35] A. Fabrocini, F. Arias de Saavedra and G. Co', *Phys. Rev. C* **61** (2000), 044302.
- [36] A. Nadasen, P. Schwandt, P.P. Singh, W.W. Jacobs, A.D. Bacher, P.T. Debevec, M.D. Kaitchuck and J.T. Meek, *Phys. Rev. C* **23** (1981), 1023.
- [37] J.R. Comfort and B.C. Karp, *Phys. Rev. C* **21** (1980), 2162.
- [38] P. Christillin, *Phys. Rep.* **190** (1990) 63.

- [39] A. Gil, J. Nieves and E. Oset, *Nucl. Phys. A* **627** (1997), 543,
J. Nacher and E. Oset, *Nucl. Phys. A* **627** (1997), 543.
- [40] J. E. Amaro, G. Co', and A. M. Lallena, *Nucl. Phys. A* **578** (1994), 365.